A&A 489, 633–650 (2008)
DOI: 10.1051/0004-6361:200810121

Astronomy & Astrophysics

Probing dust grain evolution in IM Lupi's circumstellar disc

Multi-wavelength observations and modelling of the dust disc

C. Pinte[1,2], D. L. Padgett[3], F. Ménard[2], K. R. Stapelfeldt[4], G. Schneider[5], J. Olofsson[2], O. Panić[6], J. C. Augereau[2], G. Duchêne[2,7], J. Krist[4], K. Pontoppidan[8], M. D. Perrin[9], C. A. Grady[10], J. Kessler-Silacci[11], E. F. van Dishoeck[6,12], D. Lommen[6], M. Silverstone[13], D. C. Hines[14], S. Wolf[15], G. A. Blake[8], T. Henning[16], and B. Stecklum[17]

[1] School of Physics, University of Exeter, Stocker Road, Exeter EX4 4QL, UK
e-mail: pinte@astro.ex.ac.uk
[2] Laboratoire d'Astrophysique de Grenoble, CNRS/UJF UMR 5571, 414 rue de la Piscine, BP 53, 38041 Grenoble Cedex 9, France
[3] Spitzer Science Center, Caltech, Pasadena, CA 91125, USA
[4] Jet Propulsion Laboratory, California Institute of Technology, Pasadena, CA 91109, USA
[5] Steward Observatory, The University of Arizona, 933 North Cherry Avenue, Tucson, AZ 85721, USA
[6] Leiden Observatory, Leiden University, PO Box 9513, 2300 RA Leiden, The Netherlands
[7] Astronomy Dept, UC Berkeley, Berkeley CA 94720-3411, USA
[8] Division of Geological and Planetary Sciences 150-21, California Institute of Technology, Pasadena, CA 91125, USA
[9] Department of Physics and Astronomy, UCLA, Los Angeles, CA 90095-1562, USA
[10] Eureka Scientific and Goddard Space Flight Center, Code 667, Greenbelt, MD 20771, USA
[11] The University of Texas at Austin, Department of Astronomy, 1 University Station C1400, Austin, Texas 78712–0259, USA
[12] Max Planck Institut für Extraterrestrische Physik, Giessenbachstrasse 1, 85748 Garching, Germany
[13] Eureka Scientific, Inc., NC Branch, 113 Castlefern Dr., Cary, NC 27513, USA
[14] Space Science Institute, Corrales NM, 87048, USA
[15] University of Kiel, Institute of Theoretical Physics and Astrophysics, Leibnizstrasse 15, 24098 Kiel, Germany
[16] Max Planck Institute for Astronomy, Königstuhl 17, 69117 Heidelberg, Germany
[17] Thüringer Landessternwarte Tautenburg, Sternwarte 5, 07778 Tautenburg, Germany

Received 4 May 2008 / Accepted 28 July 2008

ABSTRACT

Aims. We present a panchromatic study, involving a multiple technique approach, of the circumstellar disc surrounding the T Tauri star IM Lupi (Sz 82).
Methods. We have undertaken a comprehensive observational study of IM Lupi using photometry, spectroscopy, millimetre interferometry and multi-wavelength imaging. For the first time, the disc is resolved from optical and near-infrared wavelengths in scattered light, to the millimetre regime in thermal emission. Our data-set, in conjunction with existing photometric data, provides an extensive coverage of the spectral energy distribution, including a detailed spectrum of the silicate emission bands. We have performed a simultaneous modelling of the various observations, using the radiative transfer code MCFOST, and analysed a grid of models over a large fraction of the parameter space via Bayesian inference.
Results. We have constructed a model that can reproduce all of the observations of the disc. Our analysis illustrates the importance of combining a wide range of observations in order to fully constrain the disc model, with each observation providing a strong constraint only on some aspects of the disc structure and dust content. Quantitative evidence of dust evolution in the disc is obtained: grain growth up to millimetre-sized particles, vertical stratification of dust grains with micrometric grains close to the disc surface and larger grains which have settled towards the disc midplane, and possibly the formation of fluffy aggregates and/or ice mantles around grains.

Key words. circumstellar matter – accretion, accretion disks – planetary systems: protoplanetary disks – radiative transfer – stars: formation – pulsars: individual: IM Lupi

1. Introduction

During the first stages of planet formation following the core nucleated accretion scenario (Lissauer & Stevenson 2007), evolution of dust grains within the protoplanetary disc surrounding the central forming object is expected. Micrometre size dust grains will start to grow by coagulation during low relative velocity collisions, leading to the formation of larger, potentially fluffy aggregates (Beckwith et al. 2000; Dominik et al. 2007; Natta et al. 2007, and references therein) that will ultimately give birth to kilometre size planetesimals promoting gravitational focusing and eventually leading to planets. Timescales for the formation of these aggregates strongly depend on the physics of aggregation as well as the physical conditions within the disc, such as differential velocities between grains and grain-gas interactions.

In parallel to grain growth, dust grains are expected to settle towards the disc midplane and then to migrate inward as a result of the conjugate actions of the stellar gravity and gas drag (e.g. Barrière-Fouchet et al. 2005; Fromang & Papaloizou 2006). This settling is highly dependent on the grain size. Small grains (<1 μm) are strongly coupled to the gas, they follow its motion,

and do not settle at all. Conversely, grains in the mm-cm regime are considerably slowed down by the gas drag. They completely decouple and settle very rapidly in a thin midplane.

The result is the formation of a dust sub-disc close to the equatorial plane (e.g., Safronov & Zvjagina 1969; Dubrulle et al. 1995) that may become unstable and produce planetesimals when the density of the dust layer exceeds the gas one (e.g., Goldreich & Ward 1973; Schräpler & Henning 2004; Johansen et al. 2007). Models suggest grain growth to large particle sizes with a population of small grains remaining close to the surface and larger grains deeper in the disc (e.g. Dominik et al. 2007). However, many details of process remain uncertain. For example, it is not clear how dust grains overcome the "metre size barrier" without being accreted onto the star (e.g. Weidenschilling 1977; Brauer et al. 2008) or destroyed by high speed collisions (e.g. Jones et al. 1996; Blum et al. 2000), or how Kelvin-Helmholtz instabilities prevent the dust sublayer from fragmenting (e.g. Johansen et al. 2006).

Detection of the large building blocks of planets (particle sizes >1 m) in the disc midplane is far beyond current observational capacities, but we can expect to detect signatures of their formation. The stratified structure resulting from grain growth and settling has direct consequences on disc observables like their spectral energy distributions (SEDs) and scattered light images (e.g. Dullemond & Dominik 2004, hereafter D04). A variety of observational techniques have been used to obtain insights into the disc properties and their dust content: SEDs (e.g. D'Alessio et al. 2001), scattered light images (Watson et al. 2007), thermal emission maps in the millimetre regime (Dutrey et al. 2007), mid-infrared spectroscopy (e.g. Kessler-Silacci et al. 2006). However, each technique only provides a limited view of a disc. SED analysis leads to multiple ambiguities (e.g., Thamm et al. 1994; Chiang et al. 2001) since the lack of spatial resolution precludes from solving the degeneracies between model parameters like geometry and opacity. Spatially resolved observations in a single spectral band (scattered light in the optical or near-infrared regime or thermal emission in the millimetre domain) also gives incomplete information about the disc. As the dust opacity is a steep function of wavelength and because high temperature gradients are present within the disc, a single-band observation gives insight to only a limited region of the disc. Thus, scattered light images probe the surface layers of these optically thick discs at large radii whereas, millimetre observations are mainly sensitive to the bulk of the disc mass closer to the midplane. To precisely study fine physical processes like dust evolution and stratification, it is necessary to combine the aforementioned methods in a multi-wavelength, multiple technique observational and modelling approach.

In this paper, we study the circumstellar environment of the T Tauri star IM Lupi. The disc surrounding IM Lupi (Schwartz 82, HBC 605, IRAS 15528-3747) was first detected in scattered light with the *WFPC2* instrument on board the *Hubble Space Telescope* (*HST*) as part of a T Tauri star imaging survey (Stapelfeldt et al. 2008, in prep.). IM Lupi is an M0 T Tauri star located within the Lupus star forming clouds. It is one of four young stellar objects in the small ^{13}CO(1−0) Lupus 2 core near the extreme T Tauri star RU Lupi (Tachihara et al. 1996). Despite the low accretion-related spectroscopic activity of IM Lupi (Reipurth et al. 1996; Wichmann et al. 1999), longer wavelength observations reveal ample evidence for circumstellar material in the system with strong mm continuum emission (Nuernberger et al. 1997). Single dish ^{12}CO and ^{13}CO line observations indicate that the disc is gas rich and are consistent with a rotating disc model (van Kempen et al. 2007). The 3.3 mm continuum emission from the disc was spatially resolved by Lommen et al. (2007). Preliminary models by Padgett et al. (2006) showed that the infrared excess is well-reproduced by a disc model.

We have built a rich data set of observations of the disc: a well sampled SED, *HST* multiple wavelength scattered light images, *Spitzer* near- and mid-infrared spectroscopy and *SMA* millimetre emission maps. These observations provide different, complementary detailed views of the disc structure and dust properties. We investigate whether all of these observations can be interpreted in the framework of a single model from optical to millimetre wavelengths, and whether we can derive quantitative conclusions regarding the evolutionary stage of the disc. In Sect. 2, we describe the observations and data reduction procedure. In Sect. 3, we first draw constraints on the disc and dust properties from the various observations and then, in Sect. 4, we present simultaneous modelling of these observations. A detailed study of the dust properties is presented in Sect. 5. In Sect. 6, we discuss the implication of the results, and Sect. 7 contains the concluding remarks.

2. Observations

2.1. Scattered light images

2.1.1. HST/WFPC2 observations and data processing

HST imaging observations of the protoplanetary disc surrounding IM Lupi were obtained as part of an *WFPC2* snapshot survey of nearby T Tauri stars (*HST* Cycle 7 GO/7387 program, PI: Stapelfeldt), on 1999 February 18, using the HST Planetary Camera 1 (spatial scale of 45.5 mas pixel^{-1}). The data consist of short and long exposures through the *F606W* and *F814W* filters (*F606W*: 8 s and 100 s; *F814W*: 7 s and 80 s) which roughly correspond to Johnson *R* and *I*. The spatial resolution in both filter bands *F606W* and *F814W* is 0.06″ and 0.08″, respectively. In the long exposures, the star is heavily saturated in an attempt to reveal low surface brightness circumstellar nebulosity. After standard *WFPC2* data reduction, the stellar point spread function (PSF) was compared to our large database of *WFPC2* PSFs, and a suitable match, HD 181204, was found in field position, colour, and exposure level. The sub-pixel registration, normalisation, and subtraction of the stellar PSF was performed following the method of Krist et al. (1997). Figure 1 shows the long *F606W* and *F814W* long exposures after PSF subtraction. Obvious PSF artifacts remain in the subtracted image in the form of the saturation column bleed and residual diffraction spikes.

2.1.2. HST/NICMOS observations and data processing

Complementary near-IR observations were carried out on 2005 July 11 with the Near Infrared Camera and Multi-Object Spectrometer (*NICMOS*) as part of the *HST* Cycle 13 GO/10177 program (PI: Schneider). High contrast images of IM Lupi's circumstellar disc were obtained using *NICMOS* camera 2's coronagraphic imaging mode (spatial scale 75.8 mas pixel^{-1}) following a strategy nearly identical to that used to image the debris discs around HD 32297 (Schneider et al. 2005), HD 181327 (Schneider et al. 2006) but at a wavelength of 1.6 microns (*F160W* filter $\lambda_{\rm eff}$ = 1.604 μm, *FWHM* = 0.401 μm, spatial resolution of 0.16″).

To mitigate the potentially degrading effects of localised, but rotationally invariant, optical artifacts that appear in *NICMOS* coronagraphic images, IM Lupi was observed at two celestial

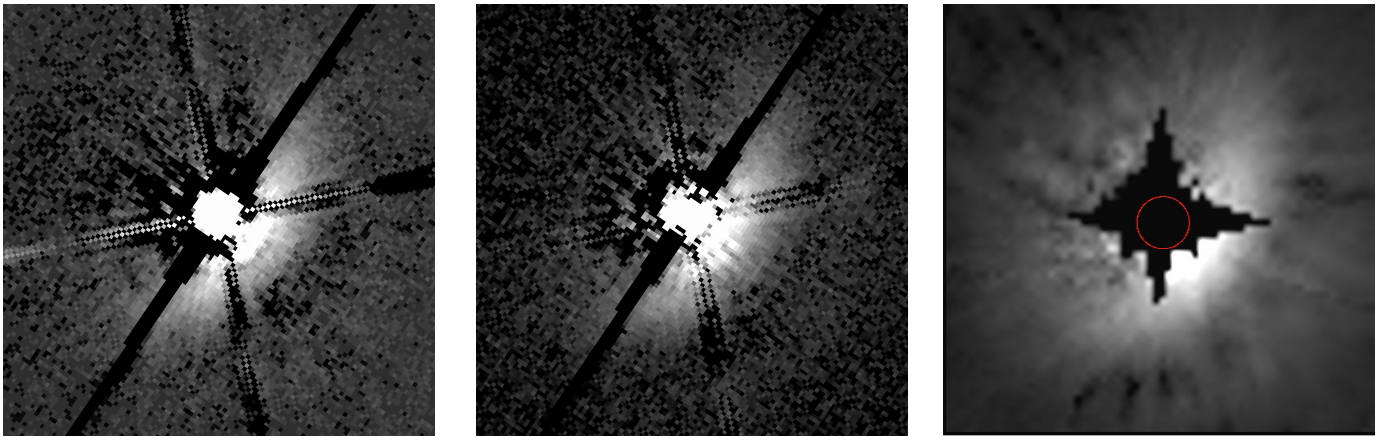

Fig. 1. The IM Lupi circumstellar disc observed in scattered light by HST. *Left and middle panels*: respectively *F606W* and F814 *WFPC2* PC1 PSF-subtracted images. The dark diagonal feature running through the star is an artifact of charge bleeding along the CCD detector columns. *Right panel*: *NICMOS* PSF-subtracted coronagraphy at 1.6 μm. The central circle represents the 0.3″ radius coronagraphic obscuration. All images are shown in square root stretch, with *North up and East to the left*. The field of view is $5 \times 5''$ (dashed boxed in Fig. 2).

orientation angles offset by 29.86°. IM Lupi was autonomously acquired and optimally positioned behind the 0.3″ radius coronagraphic obscuration following 0.241 s target acquisition imaging (also in the *F160W* filter) at each of the two spacecraft (and field) orientations. Following their respective target acquisitions, two sets of *F160W* coronagraphic observations (each yielding 704 s of integration time after median combination of count-rate images derived from three STEP32 multiaccum exposures) were obtained in a single spacecraft orbit to minimise instrumentally induced temporal variability in image structure on multi-orbit timescales. Direct (non-coronagraphic) images of IM Lupi (10.15 s), were also obtained after slewing the target out of the coronagraphic obscuration.

A set of similarly observed, high SNR, coronagraphic images of bright, isolated, non-disc bearing stars[1] observed in GO/10177, served as point spread function (PSF) templates to create PSF subtracted images of the IM Lupi disc. This process reduced the stellar light below the enhanced contrast levels provided by the coronagraph alone. The PSFs of two of the template stars with $J - H$ and $H - K$ colours similar to IM Lupi, GJ 3653 (M0.5V) and GL 517 (K5V), were well matched in structure to IM Lupi stellar PSF impressed upon the disc images. The deeply exposed *F160W* images of the PSF templates (total integration times of 1352 s and 1224 s, respectively, for GJ 3653 and GJ 517) were flux density renormalised to that of IM Lupi (based on target acquisition and direct imaging of all three stars) and used to construct four PSF subtracted images of the IM Lupi circumstellar disc (two from each orientation using both PSF templates). Residual optical artifacts arising from the *HST* secondary mirror support structure were masked in the individual PSF-subtracted images. All four images were then median combined after re-orientation to a common celestial frame to produce the then photometrically calibrated image shown in Fig. 1 (right panel) and used in the analysis discussed in this paper. For further details of the technique and process we refer the reader to the aforementioned disc imaging papers: Schneider et al. (2005) and Schneider et al. (2006).

[1] As determined from earlier (HST Cycle 7) *NICMOS* coronagraphic observations, specifically from GO/7226 for the PSF template stars discussed here.

2.1.3. Disc morphology, brightness and scattering fraction

PSF subtracted images reveal, at all wavelengths, a compact nebula adjacent to the SW of the star. Morphologically, the nebula is a broad, gentle, symmetrical arc nearly 4″ in size (celestial PA = 143° ± 5°). No clear differences are found between the nebulosity at 0.606 and 0.814 μm despite the presence of Hα and other emission lines in the *F606W* filter. In the more sensitive 1.6 micron image, the "nebulosity" is (like in the *WFPC2* images) brightest to the SW, but is clearly seen circumscribing the star. The scattered light to the NE is not apparent in the PC2 images partly due to the instrumental sensitivity limitations in PC2 PSF subtraction compared to *NICMOS* coronagraphy with PSF subtraction.

The IM Lupi images bear a striking morphological resemblance to the protoplanetary disc around the T Tauri star GM Aur (Schneider et al. 2003) and indicate the presence of a circumstellar disc inclined in the range 40–60° towards the line of sight. Because of the similar appearance of the nebula in *F606W*, *F814W* and *F160W*, with a strong front/back asymmetry, we conclude that it is dominated by scattered light from the star. To the SW of the elliptically shaped circumstellar nebulosity, an arc-like dark band (presumably the higher opacity disc midplane centered at $r \approx 1.5''$ along the disc morphological minor axis), bifurcates an isophotally concentric lower surface brightness scattering region (presumably the "lower" scattering surface of the back side of the disc) extending to $r \approx 2.5''$ on the morphological minor axis of the disc. This feature is most obvious in the *F814W* and *F160W* images. The dark lane between the upper and lower scattered light nebulae is best seen ~1.4″ southwest of the star. This coincides with the probable forward scattering direction given the purported disc inclination (see Fig. 2).

The total brightness of IM Lupi in the saturated *WFPC2* images was measured using the method of Gilliland (1994). The results are 0.088 ± 0.0044 Jy ($F606W_{\rm mag}$ = 11.44 ± 0.05) and 0.150 ± 0.0075 Jy ($F814W_{\rm mag}$ = 10.52 ± 0.05) in the *F606W* and *F814W* filters respectively. The fraction of light scattered by the disc (relative to the stellar flux at this wavelength) is 0.0186 in the *F814W* image, measured in the region beyond 0.2″ radius from the star.

From the PSF-subtracted coronagraphic image, the measured *F160W*-band disc flux density at $0.3'' > r > 4.5''$

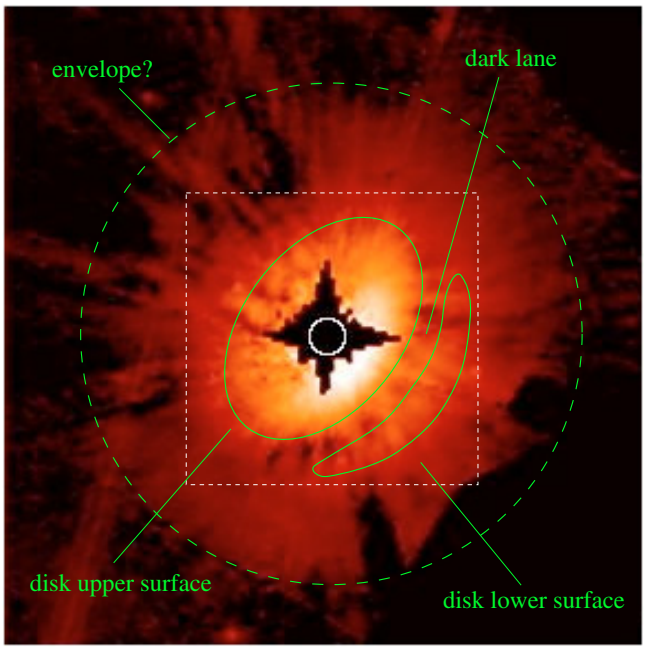

Fig. 2. *NICMOS F160W* image in log stretch. The field of view is 11 × 11″ with *North up and East to the left*. The dashed box corresponds to the field of view in Fig. 1. The central white circle represents the 0.3″ radius coronagraphic obscuration. The full green lines indicate the upper and lower scattering surfaces of the disc (separated by the dark lane which corresponds to the disc midplane). The green dashed circle represents the possible envelope surrounding the disc.

is 11.8 mJy (uncertainty ≈4%). This flux density excludes the small near-central area, shown in black in Fig. 1, which is insufficiently sampled due to masked optical artifacts. From the direct and target acquisition images we measure the *F160W*-band stellar flux density as 0.616 ± 0.012 Jy ($F160W_{\rm mag}$ = 8.11 ± 0.02) via TinyTim[2] (Krist & Hook 1997) model PSF fitting and aperture photometry. Thus, the fraction of 1.6 μm starlight scattered by the disc (beyond 0.3″ from the star) is 0.019 ± 0.001, consistent with the *F814W* value.

In the *F160W* image, a large scale fainter halo is sensitively detected to a distance of ≈4.″4 from the central star, along the morphological major axis (see Fig. 2). This large scale nebula may indicate the presence of a tentative envelope surrounding the circumstellar disc. Because the dark lane and counter nebula of the disc, which are seen through the potential envelope, are detected, this envelope must be optically thin at optical wavelengths. It is not detected in the *F606W* and *F814W* images. In the following, we focus on the disc properties and do not try to reproduce the halo in our modelling.

2.2. Spitzer IRS and MIPSSED spectra

IM Lupi was observed with the *IRS* spectrograph installed onboard the *Spitzer Space Telescope* as part of the "Cores to Discs" (*c2d*) legacy program (AOR: 0005644800, PI: Evans, Kessler-Silacci et al. 2006). The observations took place on 2004 August 30 using the four proposed modules (Short-Low, Long-Low, Short-High and Long-High), corresponding to a wavelength coverage of 5.2–38.0 μm with a spectral resolution R between 60–127 for the two "low" modules and $R \sim 600$ for the two "high" modules. The data reduction was performed using the *c2d* legacy team pipeline (Lahuis et al. 2006) with the S13 pre-reduced (BCD) data, using the aperture extraction method[3]. Pointing errors of the telescope can produce offsets between the different modules which were corrected for by the reduction pipeline. Table 1 summarises the details of the observations while the spectrum is presented in Fig. 3.

The 52–97 μm MIPSSED data ($R \sim 15$–25) were taken on 2006 March 31 (Program ID 1098, PI: Kessler-Silacci). The basic calibrated data (BCDs) were coadded using the MOsaicking and Point source EXtractor (MOPEX) software. Because the flux from IM Lupi is weak, the automated MOPEX extraction failed to extract the flux. MOPEX indeed focused on the edge of the detector, where there are a lot of hot pixels, rather than on the signal from the source. The MIPSSED spectrum was therefore extracted with IRAF since it allows the user to set the centre of the aperture (around Cols. 12–16) and performs an optimised extraction. The resulting spectrum remains too noisy to detect any spectral features, such as the 70 μm cystalline emission band. In order to increase the signal-to-noise and get a better estimate of

Table 1. Details of the *Spitzer/IRS* observations. SL, SH, LL, and LH refer to Short-Low, Short-High, Long-Low, Long-High respectively. R is the spectral resolution and *SNR* the signal to noise ratio.

Module	R	Integration time ($t_{\rm int} \times n_{\rm dce} \times n_{\rm exp}$)	*SNR*	Pointing offset (″)
SL	60–127	14 × 1 × 2	20	–0.8–0.2
SH	~600	31 × 2 × 2	71	0.7–1.3
LL	60–127	14 × 1 × 2	35	–1.4––0.3
LH	~600	60 × 1 × 2	66	3.0–1.2

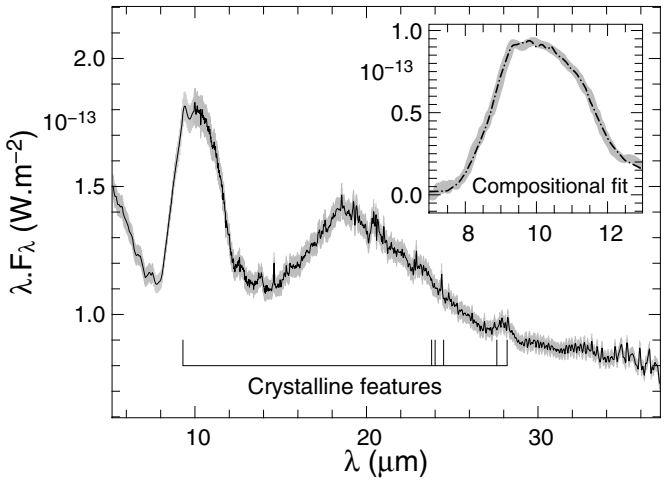

Fig. 3. *Spitzer/IRS* spectrum of IM Lupi. The large features of amorphous silicates are seen at 10 and 18 μm, as well as crystalline features at 9.3 μm and around 27 μm. A blend around 24 μm is tentatively detected. The spectrum has been slightly smoothed to reduced the noise. The jump at 20 μm is an instrumental artifact resulting from the transition between the Long-Low and Long-High modules of *IRS*. The inset shows the fit of the 10 μm continuum subtracted silicates feature. The thick grey line represents the observed spectrum (corresponding to the black line in the main panel) and the dot-dashed black line is the fitted synthetic spectrum (see Sect. 5.1).

[2] http://www.stsci.edu/software/tinytim/tinytim.html

[3] The extraction was done following two different methods: full aperture extraction and PSF extraction. PSF extraction is less sensitive to bad data samples but for some modules the estimated PSF is subpixel-sized. As a consequence, the PSF extraction becomes unstable. In this paper,we adopt the spectrum obtained with the full aperture extraction method because of its better stability.

Table 2. Photometric measurements of IM Lupi.

λ (μm)	Flux (Jy)	Date	Ref.
0.545	0.0655 ± 0.0007	06/2004	(1)
0.638	0.120 ± 0.0012	06/2004	(1)
0.797	0.216 ± 0.0022	06/2004	(1)
1.22	0.483 ± 0.0048	03/06/2000	2MASS
1.63	0.591 ± 0.0059	03/06/2000	2MASS
2.2	0.511 ± 0.0051	03/06/2000	2MASS
3.6	0.324 ± 0.0184	12/08/2004	Spitzer/IRAC
4.5	0.220 ± 0.0178	12/08/2004	Spitzer/IRAC
5.8	0.313 ± 0.0156	12/08/2004	Spitzer/IRAC
8.0	0.370 ± 0.0223	12/08/2004	Spitzer/IRAC
24	0.765 ± 0.0708	02/08/2004	Spitzer/MIPS
61.1	1.42 ± 0.22	31/03/2006	Spitzer/MIPSSED
70	1.581 ± 0.127	02/08/2004	Spitzer/MIPS
74.8	1.48 ± 0.37	02/08/2004	Spitzer/MIPSSED
89.3	1.26 ± 0.51	02/08/2004	Spitzer/MIPSSED
1300	0.1758± 0.0351	21/05/2006	SMA
3276	0.013 ± 0.0026	08/2005	(2)

References: (1) Padgett et al. (2006); (2) Lommen et al. (2007).

the mid-IR slope of the SED, we decided to bin the spectrum to calculate 3 photometric measurements at ~60, 75 and 90 μm (see Table 2).

The IRS spectrum of IM Lupi clearly shows silicate emission features typical of Class II objects (Hanner et al. 1998; Kessler-Silacci et al. 2006). In addition to the amorphous features at 10 μm (Si-O stretching mode) and 18 μm (O-Si-O bending mode), other features are visible in the spectrum that we attribute to crystalline forsterite (Mg-rich end member of the olivine group) and crystalline enstatite (Mg-rich pyroxene, Koike et al. 2000; Molster et al. 2002). The 9.3 μm feature, attributed to enstatite, is clearly visible, as is the crystalline complex at around 27 μm. This latter complex is likely a blend of a forsterite feature at 27.6 μm plus an enstatite feature at 28.2 μm (Fig. 3). A complex around 24 μm may also be tentatively detected at a signal-to-noise between 1 and 3. This complex is possibly a blend of enstatite features at 23.8 and 24.5 μm and of a forsterite feature at 24 μm. The forsterite feature at 33.6 μm is not observed.

The shape and strength of the amorphous 10 μm feature are related to the mean size of the emitting grains. These have been used as observational diagnostics for grain growth in discs (e.g. van Boekel et al. 2005; and Kessler-Silacci et al. 2006). We measured the shape and strength of the IM Lupi 10 μm feature following the approach described in Kessler-Silacci et al. (2006). The continuum normalisation is obtained using their first method. The fluxes at the reference wavelengths, $S_{11.3}$ and $S_{9.8}$, are then calculated by integrating over a wavelength range of 0.1 μm centered on λ = 9.8 μm and 11.3 μm. Finally, the feature strength is estimated by calculating the mean peak flux, $S_{\rm Peak}$, of the normalised spectrum. We obtain a $S_{11.3}/S_{9.8}$ ratio of 1.00 and a $S_{\rm Peak}$ of 1.60, which locates IM Lupi in the bulk of the class II objects observed by Kessler-Silacci et al. (2006) with a flat 10 μm feature, consistent with the presence of micron-sized grains. Overall, these features indicate a significant level of processing of the silicate grains in the disc compared to those observed in the interstellar medium, which instead are found to be submicron-sized and largely amorphous (<1% of crystalline silicates, Kemper et al. 2004).

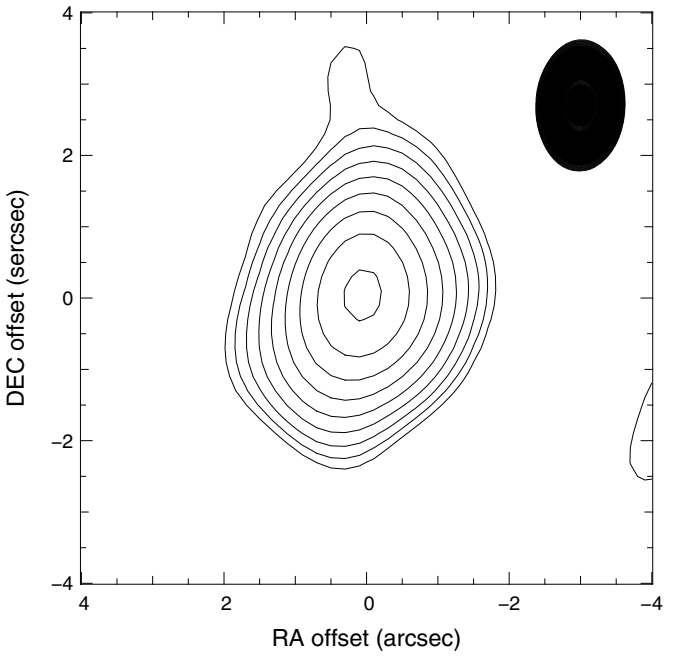

Fig. 4. *SMA* 1.30 mm aperture synthesis image of IM Lupi. Contours begin at 6 mJy/beam and step in factors of $\sqrt{2}$ in intensity. The black ellipse shows the CLEAN half-intensity beam size. The orientation is the same as in Fig. 1. The zero position is RA = 15:56:09.203, Dec = −37:56:06.40 (j2000).

2.3. Spatially resolved SMA observations of 1.3 mm continuum emission

The 1.3 mm (230.538 GHz) thermal dust emission from IM Lupi was observed with the Submillimeter Array[4] (*SMA*). See Panić et al. (in prep.) for the observational details and full analysis. The extended configuration of the *SMA*, with baselines up to 180 m, provided an excellent sampling of the *uv*-plane. The corresponding beam is 1.84″ × 1.25″, with a position angle of 0.2°.

Figure 4 presents the CLEAN map of IM Lupi's disc. The disc is clearly resolved with *FWHM*s of 2.33 × 1.72″ and a position angle of 167°. Taking into account the beam elongation, this PA is in agreement with the PA of 143° derived from scattered light images. The emission extends to ≈2″ from the star at the 3 sigma level of 6.28 mJy/beam.

The total integrated 1.3 mm flux is 175.8 ± 4 mJy. Together with the 3.3 mm flux of 13 mJy measured by Lommen et al. (2007), this leads to an estimate of the millimetre spectral index $\alpha_{\rm mm} = {\rm d}\log(F_\nu)/{\rm d}\log(\nu) = 2.80 \pm 0.25$.

Because of the relatively large noise of individual visibilities in the *uv*-plane, a direct model fitting to these is not very informative, and some form of averaging is necessary. Figure 5 shows the amplitude averaged over *uv*-distance in concentric circular annuli. We compare this amplitude with the amplitude averaged in elliptical annuli of eccentricity e = 0.65 (corresponding to a axisymmetric structure observed at an inclination of 50°). The latter is aimed at providing a more correct representation of the data, taking into account projection effects (Lay et al. 1997). The difference in amplitude for the two averaging methods is smaller than the rms levels of the observations at all baselines. Thus, the deprojection of the visibilities is not necessary in this study.

[4] The Submillimeter Array is a joint project between the Smithsonian Astrophysical Observatory and the Academia Sinica Institute of Astronomy and Astrophysics and is funded by the Smithsonian Institution and the Academia Sinica.

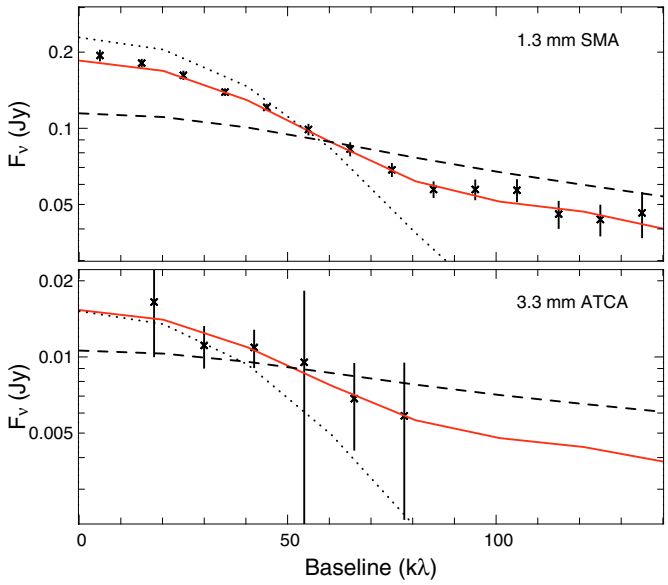

Fig. 5. Circularly averaged 1.3 mm (*upper panel*) and 3.3 mm (*lower panel*) visibility data (crosses) compared to the models (lines) with different surface density exponents. The best fit model is shown in the full red line and corresponds to $\alpha = -1$. The dashed and dotted lines correspond to the best models with $\alpha = -2$ and 0, where the inclination is enforced to be 50° (see Sect. 4.3).

In the following, we adopt the amplitude averaged in concentric circular annuli and use the same procedure to calculate the visibilities of the different models.

2.4. Spectral energy distribution

IM Lupi is an irregular variable (Batalha et al. 1998) and has been observed to flare dramatically in U band (Gahm et al. 1993). To limit the effect of variability in our analysis, we adopt the optical photometry presented by Padgett et al. (2006), which is contemporaneous to the mid-IR measurements. Mid- and far-infrared flux densities for IM Lupi were measured by the *c2d* legacy project (Evans et al. 2003). A detailed description of the reduction and source extraction procedures used for the *IRAC* and *MIPS* measurements can be found in Harvey et al. (2006, 2007) and in the *c2d* delivery document (Evans et al. 2007). All measurements are quoted in Table 2.

3. Simple estimation of some of the star and disc parameters

Each of the previously presented observations gives, by itself, strong insights into the properties of IM Lupi's disc and its dust content. Our goals in the following sections are to exploit this complete data set in order to draw complementary constraints and obtain a finer understanding of the circumstellar environment of IM Lupi and its evolutionary state. We aim at building a as coherent a picture as possible, by analysing the different observations simultaneously, in the framework of a single model.

Even with simple assumptions to describe the disc structure and dust properties, exploring the whole parameter space is far beyond current modelling capabilities. Instead, the analysis was performed in 2 steps:

1. we extract, whenever possible, parameters "directly" from observations or via simple modelling: disc size from scattered light images, disc dust mass and maximum grain size from the millimetre spectral index and dust composition from mid-infrared spectroscopy (this section). We also fit the SED alone, by a manual exploration of the parameter space, to test the need for a spatial differentiation of dust grains within the disc. The goal of this preliminary analysis is to determine which parameters can be kept fixed, allowing us to significantly reduce the dimensionality of parameter space to be explored, and which parameters need to be varied in our modelling;
2. we then systematically explore these remaining parameters, which cannot be easily extracted from observation and/or can be correlated with each other. We calculate a full grid of models and perform a simultaneous fit to all observations (Sect. 4).

3.1. Model description

Synthetic images and spectral energy distributions are computed using MCFOST, a 3D continuum radiative transfer code based on the Monte Carlo method (Pinte et al. 2006). MCFOST includes multiple scattering with a complete treatment of polarization (using the Stokes formalism), passive dust heating assuming radiative equilibrium, and continuum thermal re-emission. In short, the code first computes the temperature structure assuming that the dust is in radiative equilibrium with the local radiation field. This is done by propagating photon packets, originally emitted by the central star, through a combination of scattering (following Mie theory), absorption and reemission events until they exit the computation grid. This step uses the algorithms described in Bjorkman & Wood (2001) and Lucy (1999) with a total number of 1 280 000 photon packets. The SEDs are then computed by emitting and propagating the proper amount of stellar and disc thermal photon packets, ensuring that at least 12 800 packets are contributing in each wavelength bin. All of these packets are allowed to scatter in the disc as often as needed. We use 102 wavelength bins, globally distributed in a logarithmic scale between 0.3 and 3500 μm but with an increased resolution (linear scale with bins of 0.5 μm) between 5 and 40 μm, to properly sample the regime observed with the *IRS* spectrograph. About 4 millions packets were used to compute each of the scattered light images and thermal emission maps The maximum wavelength of *HST* observations being 1.6 μm, we assume that the disc thermal emission is negligible in the scattered light images. For the millimetre maps, both the disc thermal emission and star contribution are considered.

We consider an axisymmetric flared density structure with a Gaussian vertical profile $\rho(r,z) = \rho_0(r)\,\exp(-z^2/2\,h(r)^2)$ valid for a vertically isothermal, hydrostatic, non self-gravitating disc. We use power-law distributions for the surface density $\Sigma(r) = \Sigma_0\,(r/r_0)^{\alpha}$ and the scale height $h(r) = h_0\,(r/r_0)^{\beta}$ where r is the radial coordinate in the equatorial plane and h_0 is the scale height at the radius $r_0 = 100$ AU. The disc extends from an inner cylindrical radius $r_{\rm in}$ to an outer limit $r_{\rm out}$.

Dust grains are defined as homogeneous and spherical particles (Mie theory) with sizes distributed according to the power-law $\mathrm{d}n(a) \propto a^p\,\mathrm{d}a$, with $a_{\rm min}$ and $a_{\rm max}$ the minimum and maximum sizes of grains. Extinction and scattering opacities, scattering phase functions, and Mueller matrices are calculated using Mie theory. We adopt a power-law index $p = -3.5$, which is generally used to reproduce interstellar extinction curves. We choose a minimum grain size $a_{\rm min}$, small enough that its exact value has no effect (we fix it to 0.03 μm). The maximum grain size $a_{\rm max}$ is considered as a free parameter.

3.2. Star properties

Krautter (1992) discussed the available distance estimates for the Lupus star forming regions, ranging from 130 up to 300 pc, and concluded that the most likely distance is between the limits 130 and 170 pc. The most recent determinations are from Hughes et al. (1993), who proposed a distance of 140 ± 20 pc and from Wichmann et al. (1998), who concluded a distance of 190 ± 27 pc from *Hipparcos* parallax. In the following, we adopt this value of 190 pc and discuss the effect of distance uncertainties on the parameters derived from our modelling in Sect. 4.4.

IM Lupi has been classified as an M0 star from photometric measurements by Hughes et al. (1994). The estimated age for this system ranges from 10^5 yr to 10^7 yr (Hughes et al. 1994), depending on the pre-main sequence evolutionary track used. In the following modelling sections, we adopt a NextGen stellar atmosphere model (Allard et al. 1997) with 3900 K and $\log(g) = 3.5$, a stellar radius of $3\,R_\odot$ ($L = 1.9\,L_\odot$) and an A_V of 0.5 mag, which matches the optical photometry of IM Lupi. Following the star evolution models of Baraffe et al. (1998), this roughly corresponds to a $1\,M_\odot$ star with an age of 10^6 yr.

Hipparcos observations suggested a companion with a separation of only 0.″4 (Wichmann et al. 1998). However, neither near-IR speckle observations (Ghez et al. 1997) nor the current *HST* observations confirm the presence of a close companion. The extended nebulosity may have been marginally detected by *Hipparcos* and incorrectly interpreted in terms of a binary.

3.3. Dust composition

The strength and shape of the 10 and 20 μm emission silicate features give us some information on the dust grain composition. We find that micron sized amorphous olivine (Mg Fe SiO_4, refractive indices from Dorschner et al. 1995) dust grains reproduce in a qualitative way the emission bands. In the following general modelling approach, we do not try to match perfectly the shape of the features, but instead their strength, and we fix the composition of dust to 100% amorphous olivine. A detailed analysis of the silicates features is presented in Sect. 5.1. The results of this analysis are consistent with the composition we adopted here.

3.4. Disc outer radius

Scattered light images reveal the presence of a disc with a diameter of approximately ≈4″. The fact that we see the dark lane and the corresponding counter-nebula, produced by scattered light from the backside of the disc, indicates that the disc, if it remains optically thick at optical wavelengths, cannot extend much further away than 400 AU (assuming a distance of 190 pc). In the following we fix the outer radius in our models to 400 AU.

3.5. Disc mass

Basically, the millimetre fluxes give access to the product of the disc dust mass with the dust absorption opacity. Assuming amorphous olivine spherical grains (Dorschner et al. 1995), we obtain a maximum absorption opacity at 1.3 mm of 2 cm^2 per gram of dust, corresponding to a grain size distribution with a maximum grain size close to 3 mm. This value is also the value adopted by Beckwith et al. (1990) and more recently Andrews & Williams (2007). With this opacity, the millimetre visibilities are reproduced by a dust disc mass of $10^{-3}\,M_\odot$. This mass is estimated using the temperature structure from the solution of the radiative equilibrium. Grain size distributions with a significantly smaller or larger maximum grain size have a lower opacity at millimetre wavelengths and would imply larger disc dust masses to account for the observed fluxes. With the assumption that the gas to dust ratio is 100, as in molecular clouds, the minimum total disc mass is 0.1 $M_\odot$. With a star mass close to 1 $M_\odot$, the disc mass cannot be much larger than 0.1 $M_\odot$. We then consider it also as a maximum value and fix the disc mass to this value. It should be noted that millimetre dust opacities remain poorly known. The disc mass should thus be understood as an estimate with an uncertainty of a factor of a few.

3.6. Assessment of the need for grain size stratification

The SED of IM Lupi presents some clear features that we can use to guide our analysis on the dust properties. Our modelling confirms that the disc is almost entirely optically thin in the millimetre regime. We can therefore use the millimetre spectral index of 2.80 ± 0.25 to constrain the grain size and, thus the corresponding millimetre opacity slope is $\beta_{mm} = 0.8 \pm 0.25$. This value is significantly lower than the expected value between 1.5 and 2 for interstellar medium (ISM) grains (≤1 μm), which indicates that larger grains, of the order of 1 mm in size, are present in the disc. However, the IRS spectrum clearly shows strong silicate emission bands that cannot be reproduced by a simple power-law grain size distribution extending to millimetre sizes, even if it contains a high fraction of micron-sized grains. The silicate emission requires that the maximum grain size do not exceed a few microns in warm (close to the star), optically thin regions of the disc at mid-IR wavelengths (surface). In this section, we explore whether a dust population that is perfectly mixed with the gas, and hence uniform in the disc, can simultaneously reproduce both of these features, or whether a stratified structure with spatially separated dust populations of small and large grains is required to solve this apparent contradiction.

Assuming that the dust and gas are perfectly mixed, the silicate emission features are best reproduced with a maximum grain size $a_{max} \leq 3\,\mu$m, essentially because larger grains are featureless at mid-IR wavelengths. Figure 6 (blue dotted line) presents such a synthetic SED, with $a_{max} = 3\,\mu$m. However, this model ($\beta_{mm} = 4$) fails to reproduce the observed millimetre spectral index, as expected for grains in the Rayleigh regime. Furthermore, because of the low opacity of micron size grains in the millimetre regime, we also find a millimetre flux too low, by a factor of 10 relative to observations.

The spectral index between 1.3 and 3.3 mm suggests instead the presence of at least millimetre-sized grains. Thus, a grain size distribution with a maximum grain size close to $a_{max} = 3$ mm (Fig. 6, dashed green line) is in good agreement with our millimetre observations. This kind of grain size distribution however, does not reproduce the silicate emission features which almost completely disappear. Indeed, for a grain size distribution with a slope $p = -3.5$ and a maximum grain size ≳100 μm, the mid-IR opacities are not dominated by the sub-micron sized grains but rather by the grains a few microns in size which have featureless opacities (see for instance Fig. 5 of Kessler-Silacci et al. 2006). We can then conclude that millimetre grains are present in the disc, but that they do not dominate the opacity in regions producing silicate emission features: inner edge and disc surface at radii smaller than a few astronomical units. A spatial dependence of the dust properties, particularly grain size distribution, seems to be required to account for all observables. In the following, we assume that this spatial dependence is produced by vertical dust settling in the disc. This structure is

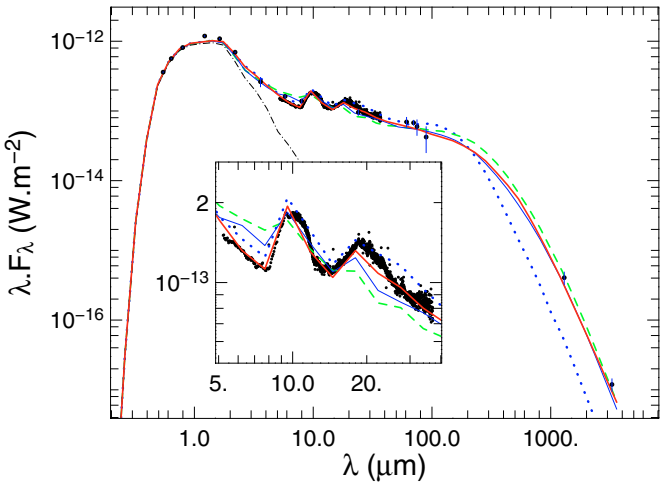

Fig. 6. Qualitative analysis of the SED of IM Lupi. The blue dotted line presents a SED calculated with submicron particles ($a_{max} = 3\,\mu$m). Silicates emission bands are well reproduced but the millimetre fluxes are too low, even with a disc mass of $M_{disc} = 0.1\,M_{\odot}$. A model with millimetre grains ($a_{max} = 3$ mm, green dashed line) performs much better at long wavelengths but the silicate features then disappear. A model including millimetre grains ($a_{max} = 3$ mm) close to the midplane and submicron grains in the upper layers (i.e. with a stratified structure as described in section 3.6), can reproduce both the silicates bands and the millimetre fluxes (red full line). The thin black dot-dash line represents the stellar photosphere.

characterised by small grains on the disc surface, which produce the silicate emission, and larger grains in the midplane which emit most of the thermal radiation in the millimetre regime. We discuss other possible explanations for the grain size stratification in Sect. 6. We describe this dust stratification by a simple parametric law, the reference scale height being a function of the grain size

$$h_{\circ}(a) = h_{\circ}(a_{min}) \left(\frac{a}{a_{min}}\right)^{-\xi}. \quad (1)$$

In the case where the dust and gas are perfectly mixed, $\xi = 0$, and $h_{\circ}(a) = h_{\circ}(a_{min})$ is independent of the grain size and is equal to the scale height of the gas disc.

The full red line in Fig. 6 presents a SED calculated with $a_{max} = 3$ mm and the stratification described above, taking $\xi = 0.1$. This kind of model reproduces both the silicate emission bands and millimetre fluxes and gives support to the presence of a stratified structure in the disc of IM Lupi. We would like to emphasise that, at this point, this model is not a fit, just an educated guess as far as disc parameters are concerned, meant only to illustrate the impact of settling on the SED. A similar effect was also found by D04 and D'Alessio et al. (2006). In the following, we fix the maximum grain size to $a_{max} = 3$ mm to match the spectral index and consider ξ as a free parameter.

4. Inferred disc model parameters from multi-technique model fitting

Encouraged by the previously described qualitative behaviour, we then moved to a quantitative analysis by exploring a full grid of models. The goal is to find a single model which self-consistently fits all observables and estimates the parameters as well as their range of validity and uncertainties. Because the *F606W* and *F814W* images are very similar, we restrict our fitting of the scattered light images to the *F606W* and *F160W* bands. Since they are the shortest and longest wavelengths: the intermediate *F814W* image is likely to be well fitted by a model that adequately represents these 2 wavelengths.

Table 3. Ranges of parameters explored in our grid of models.

Parameter	Min.	Max	N_{sampl}	Sampling
i (°)	0	90	10	linear in cos
α	–2.0	0.0	5	linear
β	1.0	1.25	6	linear
r_{in} (AU)	0.05	1.5	12	logarithmic
$h_{\circ}(a_{min})$ (AU)	8	16	13	linear
ξ	0.0	0.2	9	linear

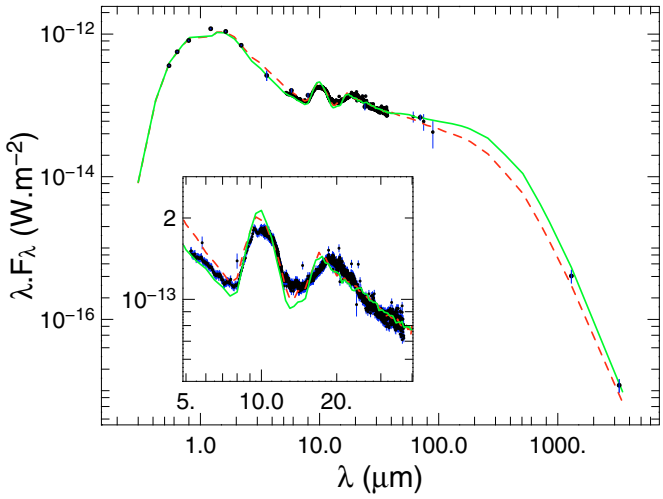

Fig. 7. SEDs of the best models. The dashed red line corresponds to best model for the fit of the SED only and the full green line corresponds to the simultaneous fit of all observations.

4.1. Explored parameter space

Exploration of the parameter space was performed by varying the geometrical properties of the disc (r_{in}, β, α, $h_{\circ}(a_{min})$) and the degree of the dust settling ξ. Scattered light images give us a good idea of the inclination angle, around 50°, but we consider it as a free parameter in order to fine tune our estimation. This results in a total of 6 independently varied parameters. The range explored for each parameter is summarised in Table 3. All combinations of parameters were explored, resulting in a total of 421 200 calculated models. The ranges were chosen to sample physically plausible values for the different parameters, and adapted during the course of the modelling to calculate all the models which may be a reasonably good representation of data. The probability curves we obtain (Fig. 9) for the different parameters show that we have sampled a large enough fraction of the parameter space.

4.2. Fitting procedure

The fitting of the SED is performed through the definition of a reduced χ^2: χ^2_{SED} from the observed and synthetic fluxes, and from the observational uncertainties. Because synthetic SEDs are sampled with a large number of packets, we neglect the model Monte Carlo error bars which are significantly smaller (<1%). We can get a sense of their amplitude in the silicate feature (inset in Fig. 7).

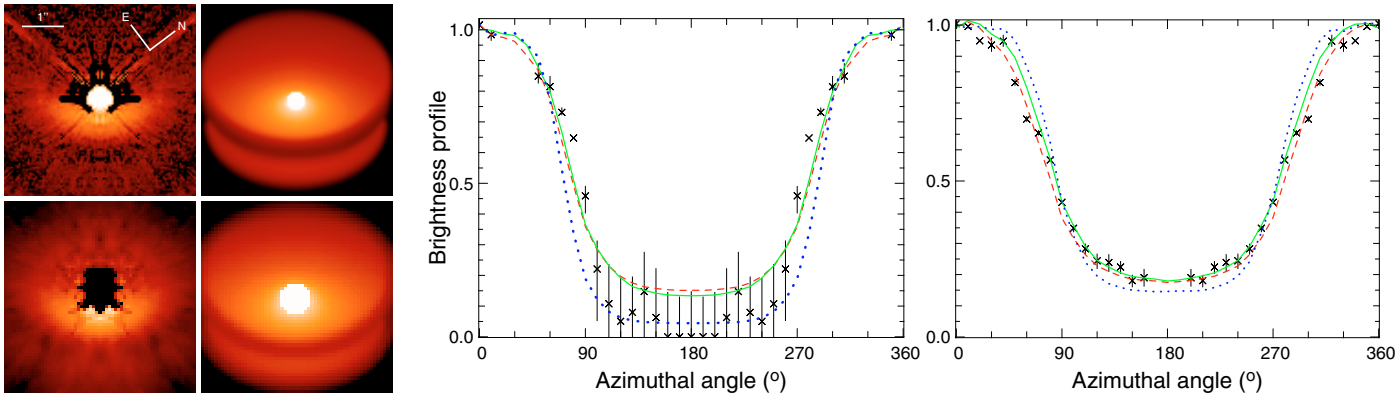

Fig. 8. Scattered light images of the best models compared to observations. *Left panel*: the *upper row* corresponds to the images at 0.606 μm and the *lower row* to those at 1.6 μm. Synthetic maps (*right*) were convolved by the core of the PSF (up to 5 pixels from the peak). *Central panel*: 0.6 μm azimuthal brightness profile. *Right panel*: 1.6 μm azimuthal brightness profile. In *both central and right panels*, the red dashed line correspond to the best fit of the scattered light only, the full green line to the best fit of all observations simultaneously and the blue dotted to the scattered light images with porous grains. The azimuthal angle is 0° in the front side of the disc, i.e. towards *bottom in the first panel*.

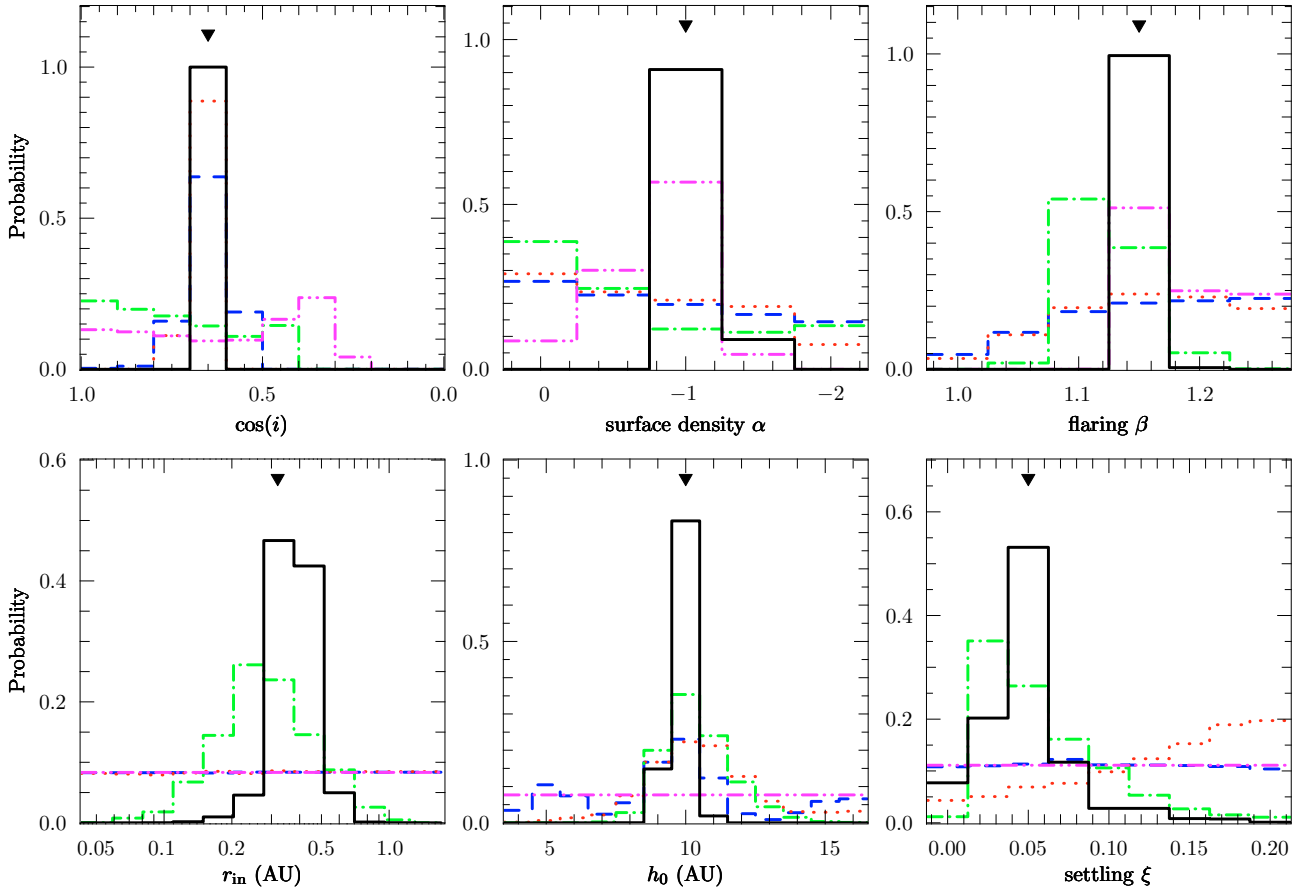

Fig. 9. Bayesian probabilities of the various parameters for the scattered light images at 0.6 μm (dashed blue) and 1.6 μm (dotted red), the SED (dot-dash green), the millimetre visibilities (dot-dot-dash pink) and for the images, SED and mm visibilities simultaneously (full black line). The triangles represent the parameters of the best model.

Comparing synthetic images with observations is a more delicate procedure due to the presence of the star that dominates the flux in the synthetic images. Observational effects are taken into account by choosing pixel sizes similar to those of observations, i.e. 0.045″/pixel at 0.6 μm and 0.076″/pixel at 1.6 μm. Real scattered light images were obtained by manual subtraction of the PSF. Such a procedure cannot be considered for the models however, given the large number of models dealt with here. To make the problem of PSF subtraction tractable, we choose to convolve our models only with the PSF core (up to 5 pixels from the peak) in order to reproduce its smoothing effect, but at the same time avoiding the superimposition of the convolved direct stellar light on the disc, where it is detected in the actual PSF-subtracted images. The disc appears left-right symmetrical in both *WFPC2* and *NICMOS* images. To increase the signal-to-noise ratio and to reduce artifacts, the observed images were symmetrised relative to the semi-minor axis of the disc, prior to comparison with models.

A pixel-by-pixel comparison between models and observations is very sensitive to observation artifacts. It requires a precise map of the observational uncertainties in the image in order to make optimal use of its information. This procedure is complex for high contrast PSF subtracted images. Large deviations in small regions of the image can strongly bias the fitting procedure. Also, PSF subtraction uncertainties introduce systematic, as opposed to random, errors, which are not properly taken into account in a χ^2 minimisation. Instead, we adopt an image fitting performed by extracting geometrical observables. Our goal here is to reproduce the main characteristics of the images, allowing small parts of the model images to not be in perfect agreement with the observations, if necessary. We therefore adopt the following method, illustrated in Fig. 8, which is based on the azimuthal intensity variations. For both wavelengths, we calculate the observed intensity variations normalised to the average flux in the azimuthal angle range $[-15°, +15°]$ (centered on the disc's semi-minor axis). For each 10° sector, we extract the average flux of the pixels encompassed between two ellipses of eccentricity $e = 0.65$ (corresponding to a circularly-symmetric structure observed at an inclination of 50°) and of semi-major axis of 1.5 and 2.1″. Regions presenting diffraction artifacts are moreover excluded from these sectors. Uncertainties were calculated by repeating the same procedure on the observations from which we have added and subtracted the estimated error maps. These error maps are constructed by taking the shot noise from photon statistics and adding in a PSF scaled by the uncertainty factor in the normalisation used for PSF subtraction.

The synthetic brightness profiles were extracted in the same way from Monte Carlo images. We do not consider any uncertainties for these synthetic profiles. For the 1.6 μm image we further use the positions of the dark lane and second nebula as geometrical observables to fit for. We compare the synthetic maps and the observations using reduced χ^2 based on the previously defined observables[5]: $\chi^2_{0.6\,\mu m}$ and $\chi^2_{1.6\,\mu m}$.

Model comparison with *SMA* and *ATCA* data was performed in (u, v) plane to avoid additional uncertainties from the image reconstruction with the CLEAN algorithm. Synthetic visibilities were computed by Fourier transform of the MCFOST emission maps. The visibilities were then binned in circular annuli as done for the observed visibilities, and the reduced χ^2 is computed from these binned visibilities: $\chi^2_{\rm mm}$. Because only 6 data points are available for the *ATCA* observations, it is not possible to define a meaningful reduced χ^2 for these observations alone. Instead, we fit simultaneously the *ATCA* and *SMA* data by defining a unique reduced χ^2. To avoid an eventual contamination by a potential envelope and/or surrounding cloud, fitting was only performed for baselines larger than 40 kλ which probe spatial scales smaller than 5″, i.e. corresponding to the disc observed in scattered light.

We compute a total $\chi^2_{\rm tot}$ defined as the sum of all the reduced χ^2:

$$\chi^2_{\rm tot} = \chi^2_{\rm SED} + \chi^2_{0.6\,\mu m} + \chi^2_{1.6\,\mu m} + \chi^2_{\rm mm}. \quad (2)$$

This $\chi^2_{\rm tot}$ allows us to do a global fitting of all observations simultaneously.

4.3. Best model

The parameters of the model with the lowest $\chi^2_{\rm tot}$ are described in Table 4. Overall, the best fit model is in very good agreement with all observations, especially taking into account the range of wavelengths and the variety of observations analysed in the fitting procedure. Table 5 shows the χ^2 corresponding to best models fitting only one of the observations and to the global best model. The global best models has χ^2 values only slightly larger than the χ^2 of the best models fitting each of the observations, showing that it offers a good representation of all observations.

The SED of this model is represented in Fig. 7. It is in very good agreement with observations from the optical to the millimetre regimes. In particular, it reproduces both the silicate bands and millimetre fluxes, and hence the millimetre spectral index. The silicates features are roughly reproduced but the shape is not exactly identical to the observed one, resulting in relatively high values of the χ^2. This is due to our very simple approximation on optical properties, with dust grains only composed of amorphous silicates. We recall here that a precise match of the silicate emission bands was not our goal at this stage of the modelling and that we were only interested in the amplitude of the silicate features.

Synthetic images of the best model are compared with observations in Fig. 8. The general shape is well reproduced at both wavelengths, with the right roundness, brightness distribution and a dark lane in good agreement with observations. The central and right panels show a quantitative comparison of the azimuthal brightness profiles. The agreement is good as shown by the values of the χ^2 in Table 5. The model predicts profiles that are very similar at both wavelengths whereas the observations suggest (given the relatively low SNR and large PSF uncertainty) a stronger contrast at 0.6 μm, with a back side compatible with a non-detection. We discuss this point in detail in Sect. 5.2.

Figure 5 shows the results of the fit of the 1.3 and 3.3 mm visibilities. The agreement is also very good for the baselines >40 kλ on which the fitting was performed. At smaller baselines, the best models are marginally below the data points.

Table 4. Best model parameters. The best model is the model with the lowest $\chi^2_{\rm tot}$. The valid range for each parameter is defined as the range of values which symmetrically enclose the central 68% of the probability (see text for details). This is equivalent to a 1σ confidence interval.

Parameter	Best model	Valid range
$T_{\rm eff}$ (K)	3900	fixed
$R_{\rm star}$ ($R_\odot$)	3.0	fixed
distance (pc)	190	fixed
$r_{\rm out}$ (AU)	400	fixed
$M_{\rm dust}$ ($M_\odot$)	10^{-3}	fixed
dust composition	100% amorphous olivine, fixed	
$a_{\rm min}$	0.03 μm	fixed
$a_{\rm max}$	3 mm	fixed
i (°)	50	45–53
surface dens. exp	–1	–0.84–−1.21
flaring exponent	1.15	1.13–1.17
$r_{\rm in}$ (AU)	0.32 AU	0.25–0.4
$h_\circ(a_{\rm min})$	10 AU	9.5–10.3
settling exponent ξ	0.05	0.02–0.07

Table 5. Reduced χ^2 values for the best models.

Model	$\chi^2_{0.6\,\mu m}$	$\chi^2_{1.6\,\mu m}$	$\chi^2_{\rm SED}$	$\chi^2_{\rm mm}$	$\chi^2_{\rm tot}$
Best 0.6 μm	**1.16**	17.24	83.47	83.60	185.47
Best 1.6 μm	3.02	**0.48**	29.75	18.64	51.89
Best SED	22.83	139.53	**9.87**	51.24	223.48
Best mm	22.69	46.13	560.75	**0.43**	630.00
Best all obs.	**1.56**	**0.68**	**14.02**	**1.18**	**17.44**

[5] A total of number of 31 and 34 measurements were used at 0.6 and 1.6 μm respectively.

This may be due to a small contamination of the observations by the surrounding molecular cloud and/or envelope. Millimetre visibilities are mainly sensitive to the apparent spatial distribution of the dust, i.e, the surface density exponent α, the disc outer radius, the total mass and the disc inclination. With an outer radius of 400 AU derived from scattered light images and a dust disc mass based on the millimetre flux, our modelling allow us to constrain the surface density profile (Fig. 5). The $\alpha = -1$ model (full line) provides an excellent match. Conversely, the other two models ($\alpha = 0$ and $\alpha = -2$) fail to successfully reproduce the data, if we force the inclination to be close to 50°. Models with $\alpha = 0$ provide a good match to the observations for a disc closer to edge-on (inclination of ≈70°), which is incompatible with the scattered light images.

In Figs. 7 and 8, we present both the overall best fit model and best fits to single observables. This quantitatively shows that the best overall fit is very similar to the individual fits and illustrates how limited single data sets are: families of models can be found that give equally good fits to the observations. It is only through a combination of the various observations that we can solve most ambiguities and disentangle between models (Fig. 9).

4.4. Validity range of parameters

To determine the range of validity of the different parameters, we use a Bayesian inference method (Press et al. 1992; Lay et al. 1997; Pinte et al. 2007). This technique allows us to estimate the probability of occurrence of each value of a given parameter. The relative probability of a point of the parameter space (i.e. one model) is given by $\exp(-\chi^2/2)$ where χ^2 refers to the previously defined reduced χ^2 of the corresponding model. All probabilities are normalised at the end of the procedure so that the sum of the probabilities of all models over the entire grid is equal to 1. This method analyses all the models in a statistical sense and does not give any specific attention to a given model, including the best model.

The Bayesian method relies on a priori probabilities on the parameters. Here, we assume that we do not have any *preliminary available information*, and we choose uniform a priori probabilities which correspond to a uniform sampling of the parameters. However, in the absence of any data, some grid points are more likely than others: consideration on solid angles show that an inclination between 80 and 90° (close to edge-on) is more likely than a inclination between 0 and 10°. Uniformly distributed disc inclinations and orientations in three dimensions correspond to a uniform distribution in the cosine of the inclination. Also, some physical quantities, like the inner radius, tend to be distributed logarithmically. The grid was built according to these distributions (Table 3).

Figure 9 presents the relative figure of merit estimated from the Bayesian inference for each of the parameters, for the fitting of the scattered light images, SED, and millimetre visibilities. These results were obtained by marginalising (i.e. summing) the probabilities of all models where one parameter is fixed successively to its different values, i.e. the probabilities of our 6-dimension parameter space are projected successively on each of the dimensions (they are not cut through the parameter space). Potential correlations between parameters are entirely accounted for with this approach, and the error bars extracted from the probability curves take into account the interplay between parameters. The resulting histograms represent the probability that a parameter takes a certain value, given the data and assumptions of our modelling.

Both scattered light images are similar and naturally lead to similar probability densities (blue dashed and red dotted lines). Because the error bars are smaller for the *NICMOS* image, the resulting constraints on the parameters are stronger. The disc inclination is well constrained in the range 45−55°. Fitting of both images tends to prefer flaring exponents ≥1.1. Because the disc is optically thick at optical and near-infrared wavelengths, scattered light images are insensitive to the surface density. These images probe the outer part of the disc, and due to the flared geometry adopted in the current work, the stellar illumination does not depend on the inner radius. As a consequence, we do not get any constraint on the inner edge of the disc. The azimuthal brightness profile is strongly sensitive to the disc scale height. Both images give slightly different, but compatible, constraints on the scale height, with a peak of probability at 10 AU. The probability curve for the 0.6 μm image also presents secondary peaks at 5 and 15 AU. These peaks correspond to the two inclination bins adjacent to the most probable bin centered at $\cos(i) = 0.65$.

The analysis of the SED gives different constraints (green dot-dash line in Fig. 9). As expected, the inclination is not well constrained. Only the models with high inclination, i.e. models that occult the star, are excluded. As the disc is very massive, it remains opaque to its own radiation up to long wavelengths, and the SED is only slightly sensitive to the disc surface density index. The flaring index, describing the disc geometry and its capacity to intercept stellar light, is strongly constrained with most probable values between 1.1 and 1.15. The inner radius is constrained between 0.15 and 0.6 AU. The probability curve for the settling index is of particular interest. The value 0, corresponding to the case without settling, has a significantly lower probability than those corresponding to a relatively low amount of settling. The peak of probability is around $\xi = 0.025$ and is followed by a decreasing probability density towards strongly settled discs. The probability becomes negligible for $\xi > 0.15$. Indeed, high degrees of settling result in silicate features that are too strong and mid-infrared fluxes that are too low. The scale height is constrained to be around 10 AU, in agreement with the modelling of the scattered light images.

The pink dot-dot-dash line shows the constraints resulting from the fitting of the millimetre visibilities. As expected, because they are mainly sensitive to the bulk of the disc mass, these observations do not give any constraints on the inner radius, scale height or degree of dust settling. Because our fitting was realised on azimuthally averaged visibilities, the inclination is not well constrained. Only the close to edge-on disc models are excluded. As previously mentioned however, the CLEAN map does give an inclination consistent with the one deduced from scattered light images. The main constraints are obtained on i) the flaring index, with the most probable value between 1.1 and 1.2, which is in agreement with the results of the SED modelling and ii) on the surface density index, with a peak of probably close to −1, and the extreme values of 0 and −2 being excluded. There is a strong correlation between the surface density index and the inclination, models with $\alpha > -1$ corresponding to inclinations >55°. Indeed, the millimetre interferometers probe the apparent spatial distribution of the dust and an inclined disc can mimic a disc with a more concentrated dust distribution.

Combined, the various observations give complementary constraints on the model parameters. Figure 9 illustrates, in a quantitative way, the complementarity between the results extracted from the scattered light images, the SED, and the millimetre visibilities. The Bayesian analysis gives the relative likelihood $p_i(M|D_i)$ of different models M, given the data D_i

(scattered light images, SED or millimetre visibilities) that have been measured. Given the n different data sets, the relative likelihood of a model is then:

$$p(M|D_1 \dots D_n) = \prod_{i=1}^{n} p_i(M|D_i), \quad (3)$$

because the uncertainties in each data set are independent. In our case, this is equivalent to calculate the probability from a $\chi^2_{\rm tot}$ we have defined as the sum of the individual reduced χ^2. The black line in Fig. 9 shows the resulting marginalised probabilities, corresponding to the simultaneous fitting of the two scattered light images, the SED, and the millimetre visibilities. All parameters are constrained within narrow ranges and the corresponding probability curves are much sharper, i.e. the constraints on the parameters are stronger (see Table 4). This illustrates the need for simultaneous modelling of various kinds of observation to quantitatively derive disc parameters and obtain finer models. Table 4 gives the range of validity of the different parameters. For each parameter θ with a density of probability $p(\theta)$, this range of validity is defined as the interval $[\theta_1, \theta_2]$ where

$$\int_{\theta_{\rm min}}^{\theta_1} p(\theta)\,{\rm d}\theta = \int_{\theta_2}^{\theta_{\rm max}} p(\theta)\,{\rm d}\theta = \frac{1-\gamma}{2} \quad (4)$$

with $\gamma = 0.68$. The interval $[\theta_1, \theta_2]$ is a 68% confidence interval and corresponds to the 1σ interval for a Gaussian density of probability.

The triangles in Fig. 9 represent the different parameters of the best model. Although this is not necessarily the case in Bayesian studies, it coincides here with the most probable model, defined as the model with the parameters which have the highest probabilities. This means that the best model corresponds to the global minimum of χ^2 in the parameter space. There is no contradiction between the constraints from the different observations indicating that our model, although based on simple assumptions, provides an adequate description (at the precision level of present observations) of the disc structure and dust properties.

4.5. Effect of distance

The results described thus far have been determined using a distance of 190 pc. It should however, be noted that the distance of IM Lupi is relatively uncertain (see Sect. 3.2). An alternate distance value will thus affect the results of our modelling. Fortunately, due to the self-similarity of the radiative transfer equations, our results can be scaled for an alternate distance. If instead the distance to IM Lupi is $A \times 190$ pc, where A is a real positive number, the calculations will be mathematically identical to the ones that we have presented if (i) all lengths in our model (star radius, disc inner and outer radius $r_{\rm in}$ and $r_{\rm out}$) are multiplied by A; (ii) the geometry is not modified (the scale height at 100 AU, flaring and surface density indices, degree of dust settling remain identical); and (iii) the disc mass is multiplied by A^2 (ensuring that the disc opacity is not modified).

5. Detailed analysis of the dust properties

In the previous section, we performed a global fit to all of the observations simultaneously. Such a fit however cannot account for the fine signatures we detect in the various observations. In this section, we analyse in detail the silicate emission bands and scattered light images to infer additional information on the dust properties.

5.1. Disc mineralogy

5.1.1. Compositional fitting of the 10 μm silicate feature

A detailed study of the 10 μm feature provides quantitative information on the composition and size of the grains responsible for the observed emission (e.g. Bouwman et al. 2001; van Boekel et al. 2005; Apai et al. 2005; Schegerer et al. 2006; or more recently Merín et al. 2007; Bouy et al. 2008; and Bouwman et al. 2008). To fit the 10 μm feature, we use five dust species: olivine (glassy Mg Fe SiO_4, Dorschner et al. 1995), pyroxene (glassy Mg Fe SiO_6, Dorschner et al. 1995) and silica (amorphous quartz (silicon dioxide) at 10K, Henning & Mutschke 1997) for the amorphous grains, and enstatite (Jaeger et al. 1998) plus forsterite (Servoin & Piriou 1973) for the crystalline species. Furthermore, we consider two single representative grain sizes (generally 0.1 and 1.5 μm, although other grain sizes have been tested) following previous studies. Once the continuum emission has been subtracted, a fit to the amorphous 10 μm feature is calculated. This is done by multiplying grain opacities with relative mass fractions and with a single-temperature blackbody. A pseudo-χ^2 minimisation procedure provides the best relative mass fractions for all of the species and grain sizes, as well as the best temperature.

Achieving a good estimation of the dust continuum emission contributing to the spectrum is the most difficult part for this sort of analysis, because it influences the derived composition. We learned from previous studies that a simple local continuum of the 10 μm feature is not a good solution, despite the fact that it is the simplest one. We find that it is necessary to leave flux at the end of the amorphous feature, at around 13.5 μm, because amorphous silicate grains are still contributing to the emission at these wavelengths. We therefore adopt the continuum produced by the MCFOST code to obtain a more realistic estimate of the continuum shape around 10 μm. Nevertheless, the best-fit disc model includes amorphous silicate grain emission, and consequently the SED is not featureless. We generated another continuum by artificially removing the amorphous features in the MCFOST calculations. Refractive indices in the wavelength range 7–35 μm, which includes the silicates features, were replaced by a log – log interpolation with wavelength of the refractive indices from the values at $\lambda = 7$ and 35 μm. This solution, although providing a more physical continuum, remains imperfect. First, the interpolated refractive indices are very likely to be a strong simplification of what would be the refractive indices without silicate features. Second, the energy normally escaping through the amorphous features is redistributed over adjacent wavelengths and this overestimates the flux near the feet of the amorphous features. A smoothing treatment is thus required to obtain a good estimate of the continuum.

5.1.2. Results

We investigated the influence of the grain size on the goodness of the fit, the result of which is that only grains of an approximate size of 1.5 μm are able to reproduce the amorphous feature (inset in Fig. 3). A first fit with grain sizes of 0.1 and 1.5 μm reveals that 94% of the grains need to have a size of 1.5 μm. A second run assuming grain sizes equal to 1.5 and 3.0 μm indicates that 97% of the grains have a size of 1.5 μm. Because 3.0 μm grains are not featureless at 10 μm, our results on the low fraction of these grains are robust. This confirms the qualitative result we obtained with the ratio $S_{11.3}/S_{9.8}$ versus the $S_{\rm Peak}$, which indicated micron-sized grains responsible for the 10 μm feature. The

result is very robust against using different continua. The derived temperature of these 1.5 μm grains is always around 350 K. The best fit is obtained for a temperature of 357 K.

In the radiative transfer modelling of the disc, the flux received by the observer in the 10 μm silicate band mainly comes from grains slightly smaller than 1 μm in size: 50% of the energy is emitted by grains between 0.1 and 1.2 μm and the the peak of the emission originates from grains 0.9 μm in size. This explains the slightly sharper silicate features in the model compared to observations (Fig. 7). The average temperature of the grains responsible for the received emission at 10 μm is 690 K, which is significantly higher than the value for the fit of the silicate feature. This may indicate that grains around 1.5 μm, responsible of most of the emission in the silicate band, are located at larger radii and/or in deeper regions than what is assumed in the global modelling. However, the large difference between temperatures should be interpreted with care and should be considered indicative only. Indeed, contrary to the global modelling, the detailed composition fit of the silicate feature has been performed after subtraction of the continuum from the MCFOST calculations (then at a temperature of 690 K). This continuum represents about 50% of the flux at a wavelength of 10 μm.

In order to reproduce the amorphous silicate feature, the fraction of crystalline grains is always less than 10%. For the best fit, the crystallinity fraction is 7%. This can mainly be explained by the presence of the enstatite feature at around 9.3 μm. Long-wavelength features, due to enstatite and forsterite grains, also indicate the presence of crystalline grains in cooler regions of the disc (larger radii and/or deeper in the disc) than the regions probed at 10 μm (Merín et al. 2007). However, these features remains weak. No features are detected at wavelengths larger than 30 μm which also suggests a low degree of crystallinity.

5.2. Are we observing fluffy aggregates?

Light scattering strongly depends on the dust properties, with the general trends that grains significantly smaller that the wavelength produce isotropic scattering and that the larger the grains the more anisotropic the scattering phase function becomes. All of IM Lupi's scattered light images present a strong front-back asymmetry indicating anisotropic scattering. This implies the presence of grains at least comparable in size with the wavelength, in the regions of the disc probed by scattered light, i.e. the disc surface at large radii ($\gtrsim$a few 10 AUs). Interestingly, the front-back flux ratio is higher at the shortest wavelength indicating that scattering could be more forward throwing in that case. Our modelling has lead to solutions that are marginally compatible with the flux level in the back side of the *F606W* image, although with a systematic overestimation (Fig. 8). In this section, we explore what kind of dust grains could produce a more contrasted azimuthal brightness profile at 0.6 μm, whilst remaining in good agreement with the azimuthal brightness profile at 1.6 μm, i.e. we try to find dust properties that could produce a flux ratio $F(180°)/F(0°)$ of 0.05 at 0.6 μm and of 0.2 at 1.6 μm (180° and 0° refer to the azimuthal angles as in Fig. 8, and not to the scattering angles). As our best model is already marginally compatible with the observations, we do not try to perform a new fit to all observations simultaneously, instead only focusing on the effect of the dust properties on the flux ratios. We adopt the geometry of the previously estimated best model. We do not consider dust settling here and take $a_{\max}$ as a free parameter. This value should now be understood as the maximum grain size in the disc surface.

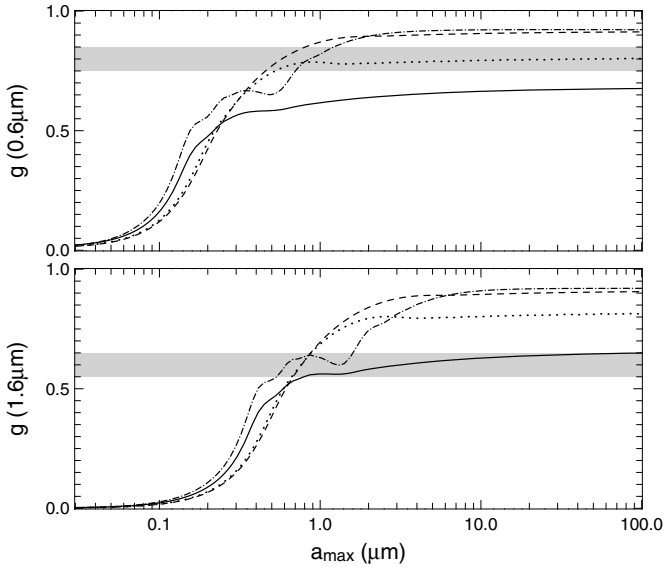

Fig. 10. Asymmetry parameter as a function of maximum grain size for different dust compositions. The *top panel* is for $\lambda = 0.6\,\mu$m and the *bottom panel* for $\lambda = 1.6\,\mu$m. The full line corresponds to the olivine compact grains used in the global modelling (slope of the grain size distribution $p = -3.5$). The dashed line corresponds to the same grains, with a porosity of 80% ($p = -3.5$). The dot-dashed line corresponds to compact grains with p = 0. The dotted line corresponds to pure water ice grains. The shaded areas represent the region that would fit the flux ratio of both the *F606W* and *F160W* scattered light images. A model reproducing both scattered light images must lie on the shaded area of both panels for the same maximum grain size.

The scattering anisotropy can be described, as a first approximation, in terms of the asymmetry parameter $g_\lambda = \langle \cos\theta_\lambda \rangle$ where θ_λ is the scattering angle at the wavelength λ. The models we have presented so far correspond to g values around 0.6 for both wavelengths, whereas for a better agreement on the flux on the backside of the disc, models with $g_{0.6\,\mu\mathrm{m}} \approx 0.8$ are needed. In Fig. 10, we plot the region ($g_{0.6\,\mu\mathrm{m}} \approx 0.8$, $g_{1.6\,\mu\mathrm{m}} \approx 0.6$) as a shaded area. This corresponds to models that would reproduce both observed azimuthal brightness profiles.

The dust grains we have used so far cannot account for the observed scattering properties, regardless of the maximum grain size (Fig. 10, full line). Indeed, they cannot result in an asymmetry parameter larger than $\approx$0.65. Within the assumption that the scattering properties of the grain can be represented with the Mie theory, there are two ways to increase the scattering anisotropy: larger grain sizes and lower refractive indices.

Then, we first tried to see whether we could reproduce the g values at both wavelengths with a different grain size distribution, by varying the slope of the distribution. We find a solution with a slope $p = 0$ (Fig. 10, dot-dash line), which is noticeably flatter than that of interstellar medium grains. This corresponds to a dust population almost devoid of very small grains (<0.1 μm). Models of dust coagulation (Dullemond & Dominik 2005; Ormel et al. 2007) show that, at least during the first stages of the process, the slope of the grain size distribution does not vary much in the regime that we are interested in. Therefore, we consider that the solution with a flat grain size distribution is unlikely to occur.

The optical properties of amorphous olivine we have used correspond to compact grains. An attractive solution to increase the scattering anisotropy is to consider porous grains, composed in a high fraction by vacuum, which will result in lower

refractive indices. The porosity is defined as the fraction of the grain volume composed of vacuum: $\mathcal{P} = V_{\rm vacuum}/V_{\rm grain} = 1 - V_{\rm solid}/V_{\rm grain}$, where $V_{\rm vacuum}$, $V_{\rm solid}$ and $V_{\rm grain}$ represent the volumes of the vacuum component, of the solid component (olivine silicates in this case) and the total volume of the grain, respectively. We calculate the optical properties of these porous grains assuming the Bruggeman effective medium mixing rule (Bruggeman 1935). The dashed line in Fig. 10 represents the multi-wavelength scattering properties of olivine grains with a porosity $\mathcal{P} = 0.8$. These grain complexes, with a maximum grain size of around 0.7 μm, mimic well the scattered properties inferred from *HST* images and in particular predict a more forward throwing scattering at 0.6 μm than at 1.6 μm (Fig. 8, blue dotted lines). We consider this as an indication that we may be observing scattered light by highly porous dust grains.

We also explored other dust compositions, in particular the porous mixture of silicates and carbon of Mathis & Whiffen (1989, model A). This model also has a porosity $\mathcal{P} = 0.8$, and the scattering properties are very similar to those of our porous olivine dust grains. This model only predicts very faint silicate emission features and cannot account for the observed *IRS* spectrum. However, this reinforces our conclusion that grains with high porosity, independently of their exact composition, may provide a good explanation for the observed brightness profiles. Interestingly, scattering properties of porous grains have been found to be a good representation of those of fluffy aggregates, as long as the size of the inclusions is in the Rayleigh regime (Voshchinnikov et al. 2005). If the inclusions are larger, then the accuracy of the effective medium theory becomes insufficient and more complex models, such as multi-layered spheres, are required to obtain a precise description of scattering properties. But the general trend, of an increase of forward throwing scattering with porosity, remains valid.

The presence of porous aggregates suggested by the scattered light images is very likely to also modify the SEDs, in particular the profile of the silicate bands, shifting the peak wavelength and affecting the shape of the bands (Min et al. 2006; Voshchinnikov & Henning 2008), as well as the dust emission in the millimetre regime (Wright 1987). Both the opacity at long wavelength (see for instance Fig. 4 in Wright 1987) and in the silicate bands are however strongly dependent on the shape of the aggregates, and not only on the degree of porosity. Voshchinnikov & Henning (2008) find that small porous grains have signatures of large grains whereas Min et al. (2006) find that large aggregates composed of small spheres have signatures of small grains. Different methods are used to represent the aggregates in both cases (multi-layered spheres and discrete dipole approximation, respectively) indicating that the micro-structure of the grains is very likely to be a key element in the opacity of aggregates.

An alternative explanation is the presence of ice mantles (H_2O, CO, ...) around dust grains. Ices have refractive indices significantly smaller than rocks ($\approx$1.3 for water ice and $\approx$1.2 for CO_2 for instance). The dust grain temperature at the surface of the disc, for radii larger than 100 AU, does not exceed 70 K, allowing the formation of such ice mantles. The dotted line in Fig. 10 presents the scattering properties of grains composed of water ice (Irvine & Pollack 1968). With a maximum grain size around 0.9 μm, these grains can also reproduce the scattering anisotropy at both wavelengths.

Current observations do not allow distinction between these two solutions (porous rock grains or grains with ice mantles). As shown in Graham et al. (2007) and Fitzgerald et al. (2007) in the case of the debris disc surrounding AU Microscopii, resolved polarimetry is a powerful tool to solve this ambiguity. Only porous grains can produce strongly anisotropic scattering and a high level of polarization.

6. Discussion

6.1. A border line CTTS but with a massive disc

IM Lupi displays only a modest amount of emission-line activity, with a Hα equivalent width which is known to vary from 7.5 to 21.5 Å (Batalha & Basri 1993). Studies of Hα emission show evidence of accretion, including variability: Reipurth et al. (1996) concluded that the Hα feature shows an inverse P Cygni profile (classification IV-Rm) and Wichmann et al. (1999) observed a III-R profile. *International Ultraviolet Explorer* low dispersion LWP spectra show that the Mg II 2798 Å line also varies, by a factor of about 2 in net flux (Valenti et al. 2003). The relatively weak emission lines and lack of optical veiling caused Finkenzeller & Basri (1987) and Martin et al. (1994) to classify this object as a weak-line T Tauri star, although our results show it would be more properly categorised as a borderline classical T Tauri star. IM Lupi is a relatively weak-lined T Tauri star with a large and massive circumstellar disc. Our modelling indicates a large dust disc mass of $M_{\rm dust} = 10^{-3}\,M_\odot$, extending up to a radius of 400 AU. This large mass is puzzling given the weakness of the Hα line, which suggests a low accretion rate. It is however possible that the diagnostics of accretion have only been observed during periods of low or moderate accretion.

6.2. Disc structure

Our multi-technique modelling allows us to quantitatively constrain most of the geometrical parameters of the disc. A flared geometry with a scale height of 10 AU at a reference radius of 100 AU is required. The best model has a midplane temperature of 14 K at 100 AU. If we assume the disc is vertically isothermal (with the temperature equal to the midplane temperature), the hydrostatic scale height $\sqrt{k_{\rm B} r^3 T(r)/GM_*\mu}$ (where μ is the mean molecular weight) is 12 and 8.5 AU, respectively, for a central mass object of 0.5 and 1 $M_\odot$, respectively. This is in good agreement with the scale height deduced from the observations (10 AU), indicating that the outer parts of the disc are very likely to be in hydrostatic equilibrium. Figure 11 presents the calculated midplane temperature compared to the temperature corresponding to the gas scale height of the best model. The agreement is very good at the inner edge and in the outer parts of the disc. In the central parts of the disc (<30 AU and excluding the very inner edge), the midplane temperature obtained in our passive disc model is too low to explain the scale height required by observations, indicating that an additional heating mechanism (like viscous heating) may be at play in the disc.

The inner radius is constrained to be between 0.25 and 0.40 AU, which corresponds to a maximum dust temperature around 1000 K. The modelling of the SED alone allows values of the inner radius down to 0.15 AU corresponding to temperatures close to the dust sublimation temperature (1500 K). The modelling of other observations gives additional constraints on the disc parameters and because of the correlations between parameters, this reduces the range of possible values for the inner radius. However, scattered images and millimetre visibilities constrain the large scale structure of the disc. Because we assume that the disc can be described in terms of power-laws from the inner edge to the outer radius, these constraints affect the derived inner radius. However, it is very likely that the description

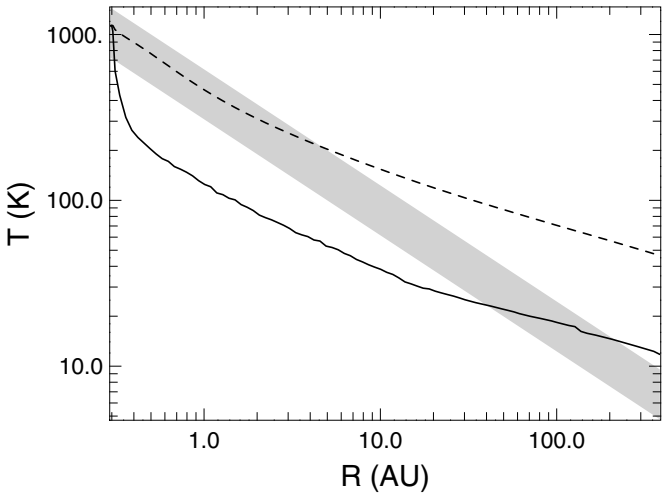

Fig. 11. Temperature structure of the disc. The full and dashed lines represent the midplane and surface temperatures, respectively. The disc surface at a given radius is defined as the altitude above the midplane where the temperature is maximal. Both temperatures become equal at the inner edge of the disc because it is directly heated by the stellar radiation. The shaded area represents the temperature corresponding to the vertical gas scale height of the best model, assuming that the disc is vertically isothermal and that the central mass is between 0.5 and 1 $M_\odot$.

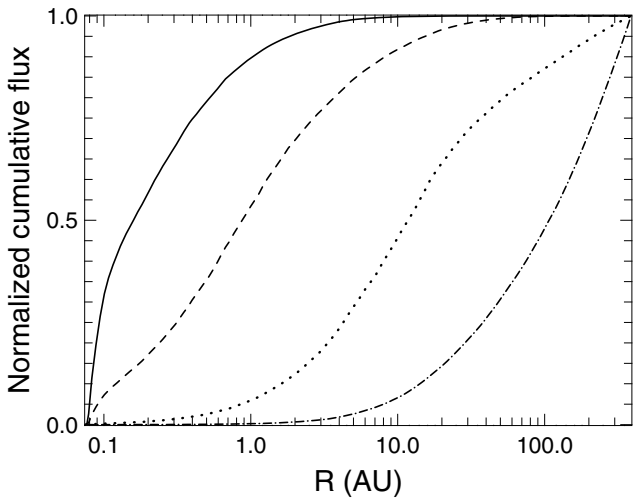

Fig. 12. Cumulative received fluxes for the best model as a function of the distance from the star at a wavelength of 10 μm (full line), 20 μm (dashed line), 70 μm (dotted line) and 1.3 mm (dot-dash line).

of the disc using power-laws is too simplistic, and more complex geometries may slightly shift the inner radius inwards, making it compatible with the dust sublimation radius.

The surface density exponent is found to be close to −1. This value corresponds to the median measurement for discs in Taurus-Aurigae obtained by Andrews & Williams (2007). This also corresponds to the theoretical value for a disc in steady-state accretion (Hartmann et al. 1998). The surface density at 5 AU is 70 g cm^{-2}. This value is within the broad peak around the median value of 14 g cm^{-2} for Taurus (Andrews & Williams 2007).

Considering a probable stellar mass of ≈1 $M_\odot$ and a gas to dust mass ratio of 100, the disc to star mass ratio is ≈0.1, meaning the disc may be unstable through gravitational collapse. The stability of the disc will depend on the surface density. Our derived value of the surface density exponent $\alpha = -1$, as opposed to values of 0 or −2, provides disc stability at all radii according to the Toomre stability criterion (Toomre 1964). Collapse of gravitationally unstable discs (Durisen et al. 2007) is one suggested mode for planet formation. The disc of IM Lupi representing about 1/10 of the star mass, local enhancement of density may be sufficient to start planet formation in the disc following this process.

Hughes et al. (2008) have shown that simultaneous studies of the dust continuum and CO emissions in several well-studied discs can be reproduced with disc models that include a tapered exponential outer edge and not a sharp outer radius as we have used here. Current observations of IM Lupi do not allow us to study in details the outer edge of the disc but the *NICMOS* image indicates that dust grains are still present at radii larger than 400 AU. However, as the counter nebulae of the disc is seen in scattered light images at 0.8 and 1.6 μm, we can get a rough estimate of the maximum value for the surface density in front of this second nebulae. Dust present at radii larger than 400 AU must be optically thin, allowing us to see the counter nebulae through the disc and the tentative envelope. This can be translated into a upper limit for the surface density of the disc[6]: $\Sigma(r \approx 500\,\mathrm{AU}) \times \kappa_{0.8\,\mu\mathrm{m}} \lesssim 1$. If we assume that the dust composition and grain size distribution are the same as in the rest of the disc, this corresponds to $\Sigma(r \approx 500\,\mathrm{AU}) \lesssim 0.2\,\mathrm{g\,cm^{-2}}$ at 500 AU, i.e. about 3.5 times smaller than the extrapolated density from our disc model, assuming it extends at radii larger than 400 AU. This implies that the density at radii larger than 400 AU must decrease significantly faster than the $1/r$ dependence we found for the disc in regions inside 400 AU.

6.3. Grain growth and dust settling

As with many other classical T Tauri stars, the slope of IM Lupi's millimetre continuum suggests a dust opacity following a law close to $\kappa_{\mathrm{abs}}(\lambda) \propto \lambda^{-1}$, indicating dust grains in the disc are larger than those in the interstellar medium. Millimetre photometry mostly traces the thermal emission of cold dust in the outer part (>15 AU) of the disc midplane (see Fig. 12), while the hot grains in the central regions contribute little to this emission.

The strong silicate features in the mid-IR spectrum indicate the presence of micron-sized grains in the disc surface inside the first central AU. The silicate emission indeed comes from the central parts of the disc: 90% of the emission at 10 and 20 μm originates from radii smaller than 1 and 10 AU, respectively (Fig. 12). Larger grains ($\gtrsim$3 μm) appear to be almost absent in these regions (Sect. 5.1).

As already mentioned, the slope of the mm continuum and the mid-IR silicate features indicate a stratified structure for the disc, with large grains in the deeper parts of the disc and small grains ($\lesssim$1 μm) in the surface of the disc. This surface layer of small grains remains difficult to characterise precisely. We have explored a structure where stratification of grain size is vertical and caused by settling of larger particles towards the disc midplane. Our model with vertical settling allows us to accurately reproduce the SED, scattered light images and millimetre emission maps. However, we cannot assess the uniqueness of the solution and other explanations may be envisaged. The warm region emitting the 10 micron silicate feature is close to the star, while the mm/submm continuum comes from the whole volume

[6] The constraint is stronger at 0.8 μm than at 1.6 μm, due to the larger dust opacity.

of the disc. We may be observing small particles close in and big grains in the outer regions of the disc. However, most physical processes: grain growth, radial drift by gas drag in the disc midplane, radiation pressure or stellar wind, will preferentially result in larger grains in the central regions and/or remove small grains from these regions. Mid-infrared interferometric observations (van Boekel et al. 2004, for HAeBe stars; and Ratzka et al. 2007; and Schegerer et al. 2008, for the T Tauri stars TW Hydra and RY Tau respectively) have confirmed these trends by showing the presence of larger and more processed grains at small spatial scales. Timescales for the production of large grains are significantly shorter in the central parts of the disc and it is difficult to imagine a physical process that will efficiently produce large grains in the outer disc without also producing them in the inner disc. Even if the current observations do not allow us to firmly conclude this point, vertical grain size stratification, probably resulting from a combination of settling and enhanced grain growth close to the midplane, appears to be a more natural explanation, and is, for now, our preferred model for the disc of IM Lupi.

Following the previously described argument, the presence of millimetre grains at large radii strongly suggests that such large grains are also present in the central AU, where the process of grain growth should be more efficient. The 10 μm features, dominated by the emission from grains of size around 1.5 μm, indicate that the mixing in the disc is sufficient to maintain micrometric grains in the disc surface. Moreover, the absence of 3 μm grains in the *IRS* spectrum indicates that the decoupling between gas and dust starts for a grain size between 1 and a few μm, i.e. grains larger than this threshold are settled below the surface $\tau_{10\,\mu m} = 1$. Given the high densities in the inner regions of the disc, an increase of 1 in optical depth is obtained over a very small spatial scale. Even a moderate amount of dust settling is sufficient to produce the observed effect. The very low values we derive for the settling index confirm that the settling remains efficiently counterbalanced by vertical mixing, due to turbulence for instance.

It is very likely that the process of dust settling evolves with different timescales as a function of the distance from the star. The silicate emission bands provide strong indications of the efficiency of dust settling as a mean of removing grains larger than a few microns from the upper layers in the central parts of the disc. The SED also gives some insights on the presence of settling in the outer parts. The *MIPS* far-IR fluxes, which are low compared to the mid-IR emission, indicate that the disc intercepts a relatively small fraction of the stellar radiation at large radii (>10 AU) compared to the fraction intercepted at radii <10 AU probed in the mid-IR (see Fig. 12). This is expected in the case of dust settling (see for instance Fig. 7 in D04). The decreasing SED of IM Lupi in the mid-infrared is very reminiscent of the models including dust settling of D04. Thus, we tried to fit the SED without taking into account the mid-infrared fluxes (between 5 and 35 μm), and hence not considering the silicate features. The resulting Bayesian probabilities still exclude models without dust settling, which do not manage to reproduce simultaneously both the millimetre and far-infrared fluxes. We conclude that dust settling is very likely to occur even in the outer regions of the disc.

D04 predicts that settled discs may become undetectable in scattered light due to the formation of a self-shadowed opacity structure in the outer disc. This is clearly not the case for IM Lupi. As noted by D04, the self-shadowed structure only appears for low values of the turbulence. This may indicate that the turbulence level in IM Lupi is large enough to prevent the disc from self-shadowing or that we are observing the outer disc at a relatively early stage of the dust settling process.

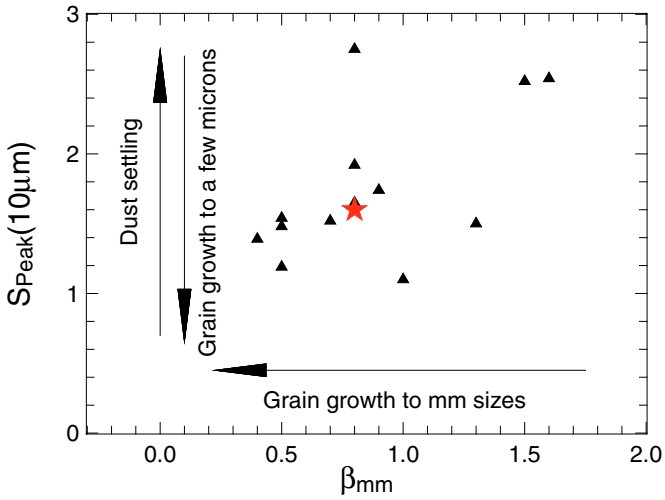

Fig. 13. Strength of the 10 μm silicate features as a function of the millimetre opacity slope for the T Tauri stars listed in Table 6. IM Lupi is represented by the red star. The effect of grain growth and dust settling are schematised by arrows.

6.4. Evolutionary state of IM Lupi and comparison with other classical T Tauri stars

Our modelling has lead to a very detailed picture of the disc surrounding IM Lupi. We have already seen that the disc structure of IM Lupi is similar to those of other classical T Tauri stars. In this section, we compare the signature of dust evolution in the disc with the results obtained for other T Tauri discs, in order to determine whether it is a singular object or whether it can be considered as representative of other T Tauri stars.

Our conclusions on the degree of dust settling in IM Lupi result from the strong silicate emission feature and shallow millimetre spectral slope. Other objects show similar characteristics. Thus, Fig. 13 presents the strength of the 10 μm silicate as a function of the exponent of the opacity law in the millimetre for a set of T Tauri stars (Table 6). IM Lupi is located in the bulk of T Tauri stars and our results can probably be extrapolated to other sources: detailed analyses of the individual sources are required, but it is likely that at least some of them are undergoing some dust settling. A semblable conclusion was reached by Furlan et al. (2005, 2006) and D'Alessio et al. (2006) based on similar evidence i.e., the presence in the SEDs of 10 and 18 μm emission silicate bands and the slope and fluxes at (sub-)millimetre wavelengths.

The tentative correlation between the strength of the silicate feature and millimetre spectral index suggested by Lommen et al. (2007) does not appear as clear in our larger sample of T Tauri stars. This correlation was interpreted as an indication of fast grain growth in both central and outer regions of the disc. Indeed, as grains grow from sub-micron sizes to several microns, the 10 μm feature becomes weaker and less peaked. When they reach millimetre to centimetre sizes, the slope of the millimetre emission becomes shallower. But, as we have shown, the strength of the silicate features is strongly related to the degree of dust settling. The stronger the settling, the smaller the apparent (i.e. probed in the infrared) grain size, making it difficult to obtain a precise estimate of the actual grain sizes present in the midplane.

Table 6. Millimetre opacity slopes and strengths of the 10 μm silicate features of T Tauri stars.

Name	β_{mm}	$S_{Peak}(10\,\mu m)$	Ref.
IM Lup	0.8 ± 0.25	1.60	this work
HT Lup	0.4 ± 0.5	1.39	(1, 2)
GW Lup	0.5 ± 0.5	1.48	(1, 2)
CR Cha	1.5 ± 0.6	2.52	(1, 3)
WW Cha	0.8 ± 0.8	1.92	(1, 3)
RU Lup	0.8 ± 0.5	1.54	(1, 2)
RY Tau	0.8 ± 0.1	2.75	(4, 5)
FT Tau	0.9 ± 0.3	1.74	(4, 5)
DG Tau	0.7 ± 0.1	1.52	(4, 5)
UZ Tau E	0.8 ± 0.1	1.65	(4, 5)
DL Tau	1.0 ± 0.2	1.1	(4, 5)
CI Tau	1.3 ± 0.4	1.5	(4, 5)
DO Tau	0.5 ± 0.1	1.19	(4, 5)
GM Aur	1.6 ± 0.2	2.54	(4, 5)

References: (1) Lommen et al. (2007); (2) Kessler-Silacci et al. (2006); (3) Przygodda et al. (2003); (4) Rodmann et al. (2006); (5) Furlan et al. (2006). The source T Cha presented in Lommen et al. (2007) was not selected, because of the presence of PAH emission. Both Rodmann et al. (2006) and Lommen et al. (2007) take a contribution of optically thick emission into account in their derivation of β_{mm}.

The detailed analysis of the silicate features indicates a small degree of crystallisation (<10%) in spite of a high mass fraction of micrometric (hence evolved) grains. As shown by Schegerer et al. (2006, see their Fig. 9 for instance), this is the case for several objects and IM Lupi is not unique on that aspect. Schegerer et al. (2006) did not find any correlation between the degree of crystallisation and amount of micron-sized grains.

Furlan et al. (2005, 2006) and D'Alessio et al. (2006) have estimated the degree of dust settling based on the colours and SEDs of a large population of Classical T Tauri stars in the Taurus molecular cloud. They claim that to make a synthetic SED consistent with the median SED of class II objects in Taurus, the dust to gas mass ratio in the disc atmosphere should be around 1% (between 0.1 and 10%) of the ISM ratio. In our modelling, the grain size distribution and the dust to gas ratio are continuous functions of the height above the midplane. With $\xi = 0.05$, the dust to gas ratio starts at 1.5 times the ISM value in the disc midplane and reaches 10%, 1% and 0.1% of the ISM value at 2, 3 and 6 scale heights, respectively. These regions roughly correspond to what is defined as the disc surface in Furlan et al. (2005, 2006) and D'Alessio et al. (2006). Although not directly comparable, our estimation of the degree of dust settling appears consistent with the calculations of these authors.

7. Summary

We have constructed a high quality data set of the circumstellar disc of IM Lupi, spanning a wide range of wavelengths, from the optical to the millimetre. All of these observations can be interpreted in the framework of single model. A Bayesian analysis of a large grid of models allows us to establish strong constraints on all the parameters of the model. Although each individual observation provides valuable information on the disc, the presented method clearly illustrates the need for multi-wavelength and multi-technique studies in order to obtain finer understanding of protoplanetary discs. The conclusions of this work are:

1. The disc structure is very well constrained. The disc extends from an inner radius <0.4 AU, compatible with the dust sublimation radius, up to 400 AU. The scale height is 10 AU at 100 AU and varies with a flaring index of 1.15, indicating that the disc is in hydrostatic equilibrium in its outer parts. The slope of the surface density is confined to values close to −1, which is in agreement with the median value of Andrews & Williams (2007) and predictions of steady-state accretion disc models.
2. The millimetre spectral index indicates that grains have grown up to a few millimetre in sizes in the disc midplane.
3. The strong silicate emission bands, probing the surface of the disc in the central few AUs, also present signatures of dust evolution. They are dominated by grains around 1.5 μm but are almost devoid of grains larger than 3 μm.
4. We conclude that a spatial stratification of the dust grains, depending on their size is present in the disc. The disc of IM Lupi has probably entered the first phases of planetary formation: dust grains with sizes several orders of magnitude larger than interstellar grains are present in the disc and dust settling is probably occurring, at least in the central parts but potentially also in the outer regions of the disc. Models without dust settling are excluded but the settling is constrained to a low value, suggesting that mixing, by turbulence for instance, remains efficient in the disc.
5. IM Lupi presents signatures of crystalline grains but with a low overall degree of crystallinity (<10%). This is in agreement with the results of Schegerer et al. (2006) who found that grain growth and crystallisation occurs simultaneously in T Tauri discs, although grain growth is dominant.
6. The simultaneous analysis of the 0.6 and 1.6 μm scattered light images suggests that light scattering can be more forward throwing at short wavelengths. Although the data are marginally compatible with compact silicate grains, this could indicate the presence of grains with low refractive indices. They may be fluffy aggregates (porous grains) and/or the result of the formation of ice mantles around grains. Both phenomena are expected to occur in discs and additional information (like polarisation) is required to distinguish between them.

The combination of our observations and modelling makes IM Lupi one of the best studied protoplanetary disc surrounding a solar mass star. With the exception of its low accretion signatures, all of the observations indicate that IM Lupi is a typical classical T Tauri star. Although significant differences are expected between individual objects, IM Lupi can probably be considered as good prototype of protoplanetary discs for further studies.

Acknowledgements. Authors would like to thank T. Hill for valuable comments on the manuscript. Computations presented in this paper were performed at the Service Commun de Calcul Intensif de l'Observatoire de Grenoble (SCCI) and on the University of Exeter's SGI Altix ICE 8200 supercomputer. C. Pinte acknowledges the funding from the European Commission's Seventh Framework Program as a Marie Curie Intra-European Fellow (PIEF-GA-2008-220891). The authors thank the *Programme National de Physique Stellaire* (PNPS) and *l'Action Spécifique en Simulations Numériques pour l'Astronomie* (ASSNA) of CNRS/INSU, France and Agence Nationale pour la Recherche (ANR) of France under contract ANR-07-BLAN-0221, for supporting part of this research. This investigation was based, in part, on observations made with the NASA/ESA Hubble Space Telescope, obtained at the Space Telescope Science Institute (STScI), which is operated by the Association of Universities for Research in Astronomy, Inc., under NASA contract NAS 5-26555. These observations are associated with programs G0/7387 and GO/10177. Support for these programs was provided by NASA through grants from STScI. This research has made use of the SIMBAD database, operated at CDS, Strasbourg, France, and data from the Two Micron All Sky Survey (U. Mass, IPAC/CIT) funded by NASA and NSF. Support for this work, part of the Spitzer Postdoctoral Fellowship Program, was provided by NASA through contracts 1224608, 1230779 and 1256316, issued by

the Jet Propulsion Laboratory, California Institute of Technology, under NASA contract 1407. Astrochemistry in Leiden is supported by a NWO Spinoza grant and a NOVA grant, and by the European Research Training Network "The Origin of Planetary Systems" (PLANETS, contract number HPRN-CT-2002-00308).

References

Allard, F., Hauschildt, P. H., Alexander, D. R., & Starrfield, S. 1997, ARA&A, 35, 137
Andrews, S. M., & Williams, J. P. 2007, ApJ, 659, 705
Apai, D., Pascucci, I., Bouwman, J., et al. 2005, Science, 310, 834
Baraffe, I., Chabrier, G., Allard, F., & Hauschildt, P. H. 1998, A&A, 337, 403
Barrière-Fouchet, L., Gonzalez, J.-F., Murray, J. R., Humble, R. J., & Maddison, S. T. 2005, A&A, 443, 185
Batalha, C. C., & Basri, G. 1993, ApJ, 412, 363
Batalha, C. C., Quast, G. R., Torres, C. A. O., et al. 1998, A&AS, 128, 561
Beckwith, S. V. W., Henning, T., & Nakagawa, Y. 2000, Protostars and Planets IV, 533
Beckwith, S. V. W., Sargent, A. I., Chini, R. S., & Guesten, R. 1990, AJ, 99, 924
Bjorkman, J. E., & Wood, K. 2001, ApJ, 554, 615
Blum, J., Wurm, G., Kempf, S., et al. 2000, Phys. Rev. Lett., 85, 2426
Bouwman, J., Meeus, G., de Koter, A., et al. 2001, A&A, 375, 950
Bouwman, J., Henning, T., Hillenbrand, L. A., et al. 2008, ArXiv e-prints, 802
Bouy, H., Huélamo, N., Pinte, C., et al. 2008, A&A, submitted
Brauer, F., Dullemond, C. P., & Henning, T. 2008, A&A, 480, 859
Bruggeman, D. 1935, Ann. Phys., 24, 636
Chiang, E. I., Joung, M. K., Creech-Eakman, M. J., et al. 2001, ApJ, 547, 1077
D'Alessio, P., Calvet, N., & Hartmann, L. 2001, ApJ, 553, 321
D'Alessio, P., Calvet, N., Hartmann, L., Franco-Hernández, R., & Servín, H. 2006, ApJ, 638, 314
Dominik, C., Blum, J., Cuzzi, J. N., & Wurm, G. 2007, in Protostars and Planets V, ed. B. Reipurth, D. Jewitt, & K. Keil, 783
Dorschner, J., Begemann, B., Henning, T., Jaeger, C., & Mutschke, H. 1995, A&A, 300, 503
Dubrulle, B., Morfill, G., & Sterzik, M. 1995, Icarus, 114, 237
Dullemond, C. P., & Dominik, C. 2004, A&A, 421, 1075
Dullemond, C. P., & Dominik, C. 2005, A&A, 434, 971
Durisen, R. H., Boss, A. P., Mayer, L., et al. 2007, in Protostars and Planets V, ed. B. Reipurth, D. Jewitt, & K. Keil, 607
Dutrey, A., Guilloteau, S., & Ho, P. 2007, in Protostars and Planets V, ed. B. Reipurth, D. Jewitt, & K. Keil, 495
Evans, N. J., Allen, L. E., Blake, G. A., et al. 2003, PASP, 115, 965
Evans, N. J., Harvey, M. M., Huard, T. L., et al. 2007, Final Delivery of Data from the c2d Legacy Project: IRAC and MIPS, Tech. rep. (Pasadena: Spitzer Science Center) http://data.spitzer.caltech.edu/popular/c2d
Finkenzeller, U., & Basri, G. 1987, ApJ, 318, 823
Fitzgerald, M. P., Kalas, P. G., Duchêne, G., Pinte, C., & Graham, J. R. 2007, ApJ, 670, 536
Fromang, S., & Papaloizou, J. 2006, A&A, 452, 751
Furlan, E., Calvet, N., D'Alessio, P., et al. 2005, ApJ, 628, L65
Furlan, E., Hartmann, L., Calvet, N., et al. 2006, ApJS, 165, 568
Gahm, G. F., Gullbring, E., Fischerstrom, C., Lindroos, K. P., & Loden, K. 1993, A&AS, 100, 371
Ghez, A. M., McCarthy, D. W., Patience, J. L., & Beck, T. L. 1997, ApJ, 481, 378
Gilliland, R. L. 1994, ApJ, 435, L63
Goldreich, P., & Ward, W. R. 1973, ApJ, 183, 1051
Graham, J. R., Kalas, P. G., & Matthews, B. C. 2007, ApJ, 654, 595
Hanner, M. S., Brooke, T. Y., & Tokunaga, A. T. 1998, ApJ, 502, 871
Hartmann, L., Calvet, N., Gullbring, E., & D'Alessio, P. 1998, ApJ, 495, 385
Harvey, P., Merín, B., Huard, T. L., et al. 2007, ApJ, 663, 1149
Harvey, P. M., Chapman, N., Lai, S.-P., et al. 2006, ApJ, 644, 307
Henning, T., & Mutschke, H. 1997, A&A, 327, 743
Hughes, A. M., Wilner, D. J., Qi, C., & Hogerheijde, M. R. 2008, ArXiv e-prints, 801
Hughes, J., Hartigan, P., & Clampitt, L. 1993, AJ, 105, 571
Hughes, J., Hartigan, P., Krautter, J., & Kelemen, J. 1994, AJ, 108, 1071
Irvine, W. M., & Pollack, J. B. 1968, Icarus, 8, 324
Jaeger, C., Molster, F. J., Dorschner, J., et al. 1998, A&A, 339, 904
Johansen, A., Henning, T., & Klahr, H. 2006, ApJ, 643, 1219
Johansen, A., Oishi, J. S., Low, M.-M. M., et al. 2007, Nature, 448, 1022
Jones, A. P., Tielens, A. G. G. M., & Hollenbach, D. J. 1996, ApJ, 469, 740
Kemper, F., Vriend, W. J., & Tielens, A. G. G. M. 2004, ApJ, 609, 826
Kessler-Silacci, J., Augereau, J.-C., Dullemond, C. P., et al. 2006, ApJ, 639, 275
Koike, C., Tsuchiyama, A., Shibai, H., et al. 2000, A&A, 363, 1115
Krautter, J. 1992, The Star Forming Region in Lupus, Low Mass Star Formation in Southern Molecular Clouds, 127
Krist, J. E., & Hook, R. N. 1997, in The 1997 HST Calibration Workshop with a New Generation of Instruments, ed. S. Casertano, R. Jedrzejewski, T. Keyes, & M. Stevens, 192
Krist, J. E., Burrows, C. J., Stapelfeldt, K. R., & WFPC2 Id Team 1997, BAAS, 29, 1215
Lahuis, F., Kessler-Silacci, J. E., Evans, N. J., I., et al. 2006, c2d Spectroscopy Explanatory Supplement, Tech. rep. (Pasadena: Spitzer Science Center)
Lay, O. P., Carlstrom, J. E., & Hills, R. E. 1997, ApJ, 489, 917
Lissauer, J. J., & Stevenson, D. J. 2007, in Protostars and Planets V, ed. B. Reipurth, D. Jewitt, & K. Keil, 591
Lommen, D., Wright, C. M., Maddison, S. T., et al. 2007, A&A, 462, 211
Lucy, L. B. 1999, A&A, 345, 211
Martin, E. L., Rebolo, R., Magazzu, A., & Pavlenko, Y. V. 1994, A&A, 282, 503
Mathis, J. S., & Whiffen, G. 1989, ApJ, 341, 808
Merín, B., Augereau, J.-C., van Dishoeck, E. F., et al. 2007, ApJ, 661, 361
Min, M., Dominik, C., Hovenier, J. W., de Koter, A., & Waters, L. B. F. M. 2006, A&A, 445, 1005
Molster, F. J., Waters, L. B. F. M., & Tielens, A. G. G. M. 2002, A&A, 382, 222
Natta, A., Testi, L., Calvet, N., et al. 2007, in Protostars and Planets V, ed. B. Reipurth, D. Jewitt, & K. Keil, 767
Nuernberger, D., Chini, R., & Zinnecker, H. 1997, A&A, 324, 1036
Ormel, C. W., Spaans, M., & Tielens, A. G. G. M. 2007, A&A, 461, 215
Padgett, D. L., Cieza, L., Stapelfeldt, K. R., et al. 2006, ApJ, accepted [arXiv:astro-ph/0603370]
Pinte, C., Ménard, F., Duchêne, G., & Bastien, P. 2006, A&A, 459, 797
Pinte, C., Fouchet, L., Ménard, F., Gonzalez, J.-F., & Duchêne, G. 2007, A&A, 469, 963
Press, W. H., Teukolsky, S. A., Vetterling, W. T., & Flannery, B. P. 1992, Numerical recipes. The art of scientific computing (Cambridge University Press), 2nd edn.
Przygodda, F., van Boekel, R., Àbrahàm, P., et al. 2003, A&A, 412, L43
Ratzka, T., Leinert, C., Henning, T., et al. 2007, A&A, 471, 173
Reipurth, B., Pedrosa, A., & Lago, M. T. V. T. 1996, A&AS, 120, 229
Rodmann, J., Henning, T., Chandler, C. J., Mundy, L. G., & Wilner, D. J. 2006, A&A, 446, 211
Safronov, V. S., & Zvjagina, E. V. 1969, Icarus, 10, 109
Schegerer, A., Wolf, S., Voshchinnikov, N. V., Przygodda, F., & Kessler-Silacci, J. E. 2006, A&A, 456, 535
Schegerer, A. A., Wolf, S., Ratzka, T., & Leinert, C. 2008, A&A, 478, 779
Schneider, G., Wood, K., Silverstone, M. D., et al. 2003, AJ, 125, 1467
Schneider, G., Silverstone, M. D., & Hines, D. C. 2005, ApJ, 629, L117
Schneider, G., Silverstone, M. D., Hines, D. C., et al. 2006, ApJ, 650, 414
Schräpler, R., & Henning, T. 2004, ApJ, 614, 960
Servoin, J., & Piriou, B. 1973, Phys. Stat. Sol. (b), 55, 677
Tachihara, K., Dobashi, K., Mizuno, A., Ogawa, H., & Fukui, Y. 1996, PASJ, 48, 489
Thamm, E., Steinacker, J., & Henning, T. 1994, A&A, 287, 493
Toomre, A. 1964, ApJ, 139, 1217
Valenti, J. A., Fallon, A. A., & Johns-Krull, C. M. 2003, ApJS, 147, 305
van Boekel, R., Min, M., Leinert, C., et al. 2004, Nature, 432, 479
van Boekel, R., Min, M., Waters, L. B. F. M., et al. 2005, A&A, 437, 189
van Kempen, T. A., van Dishoeck, E. F., Brinch, C., & Hogerheijde, M. R. 2007, A&A, 461, 983
Voshchinnikov, N. V., & Henning, T. 2008, A&A, 483, L9
Voshchinnikov, N. V., Il'in, V. B., & Henning, T. 2005, A&A, 429, 371
Watson, A. M., Stapelfeldt, K. R., Wood, K., & Ménard, F. 2007, in Protostars and Planets V, ed. B. Reipurth, D. Jewitt, & K. Keil, 523
Weidenschilling, S. J. 1977, MNRAS, 180, 57
Wichmann, R., Bastian, U., Krautter, J., Jankovics, I., & Rucinski, S. M. 1998, MNRAS, 301, L39
Wichmann, R., Covino, E., Alcalá, J. M., et al. 1999, MNRAS, 307, 909
Wright, E. L. 1987, ApJ, 320, 818